Electroosmotic flow in soft microchannels at high grafting densities

Arman Sadeghi,[1,*] Milad Azari,[1,†] and Steffen Hardt[2,‡]
[1]*Department of Mechanical Engineering, University of Kurdistan, Sanandaj 66177-15175, Iran*
[2]*Institute for Nano- and Microfluidics, TU Darmstadt, 64287 Darmstadt, Germany*

(Received 6 February 2019; published 24 June 2019)

This paper reports the results of a theoretical modeling of the fully developed electroosmotic flow in a rectangular microchannel with a high-density polyelectrolyte layer (PEL) attached to the walls. At these conditions, the ions are partitioned between the PEL and the fluid outside the PEL owing to the difference between the permittivities of the two media. It is taken into account that the dynamic viscosity is higher within the PEL because of hydration effects. Solutions are obtained for the electric potential and velocity distributions as well as the mean velocity by making use of a variational approach, applied to the linearized form of the governing equations, which treats the whole area under consideration as a single domain with variable physical properties. The resulting equations are solved using a spectral method. Closed-form analytical expressions are obtained for a slit geometry, representing the case of high aspect ratios. The solutions obtained are validated by comparing to finite-element simulations of the full nonlinear equations. It is shown that the electric potential drop inside the channel increases due to the depletion of the counterions within the PEL caused by the ion partitioning effect. This effect, surprisingly, magnifies the electroosmotic flow rate because of the increase of the space charge outside the PEL. As expected, the hydration effects reduce the flow rate, especially for thick PELs.

DOI: 10.1103/PhysRevFluids.4.063701

I. INTRODUCTION

Unlike fluid flow in macroscopic ducts, in microchannels liquid flow is often driven by electric fields instead of pressure gradients. One of the main underlying reasons is the unfavorable scaling of pressure-driven flow with the channel diameter. Electroosmotic flow (EOF) is caused by the body force an electric field exerts on the space-charge layer forming in the vicinity of surfaces, termed the electric double layer (EDL). Although the ions located in the inner layer are attached to the surface, those within the outer diffuse layer can move under the influence of an electric field. The ionic movement within the diffuse layer due to an applied electric field results in momentum transfer to the liquid molecules through viscous drag, creating a net fluid flow called electroosmosis [1].

Electroosmotic pumps are now considered one of the prominent microfluidic actuators. Apart from the more favorable scaling of the flow rate with the channel diameter than pressure-driven devices, there are other reasons for such achievements, including the fact that the electroosmotic micropumps do not possess moving parts, rendering their design and fabrication much easier than many of their counterparts [2]. Furthermore, the pluglike velocity profile makes it possible to transport samples with minimum dispersion [3].

*Corresponding author: a.sadeghi@eng.uok.ac.ir
†m.azari@eng.uok.ac.ir
‡hardt@nmf.tu-darmstadt.de

The electroosmotic velocity is dependent on different parameters like the applied electric field strength, the fluid properties, and the wall zeta potential. For a given fluid, the velocity may be increased by increasing either the electric field strength or the zeta potential. However, increasing the electric field results in more Joule heating which may lead to denaturation of samples in biomicrofluidic devices. Moreover, the temperature gradients arising from Joule heating can cause band spreading of the samples [4]. Hence, often the only practical way of increasing the flow rate is to choose materials with high zeta potentials. In many cases, however, the design objectives are not met by the native properties of the materials. For such cases, it is possible to alter the surface properties in order to attain the desired flow characteristics. One of the most successful ways of surface treatment is to apply polyelectrolyte layer (PEL) coatings, which often consists of grafting polymer brushes containing electrically charged groups to the surface [5]. Such brushes are formed when polymer chains are densely grafted to a surface, forcing them to stretch along the direction normal to the surface to avoid overlapping each other [6]. The presence of the polyelectrolyte (PE) brushes in a channel modifies the fluid flow in a twofold manner. First, the brushes exert a resistive force on the fluid that tends to retard the flow. Second, the fixed-charge groups located on the brushes attract ions of opposite sign, thereby altering the charge distribution and, ultimately, the electroosmotic flow. By appropriately adjusting the above-mentioned effects, it may be possible to obtain the desired flow characteristics [7]. Alternatively, the coating may consist of PE multilayers that are created by physisorption of polyelectrolytes to a surface [8].

One of the first theoretical studies related to EOF in PEL-coated conduits (also called soft channels) was performed by Donath and Voigt [9]. They proposed expressions for the streaming potential and the surface conductivity associated with a pressure-driven flow between two parallel plates. Shortly thereafter, a theory was developed by Ohshima and Kondo [10] for electrokinetic flow between two parallel plates covered by ion-penetrable charged layers, considering a uniform distribution of the fixed-charge groups. More recently, an equation was derived by Starov and Solomentsev [11] for the streaming potential in coated capillaries by incorporating the influence of the ionic diffusion along the capillary. In a paper by Keh and Liu [12], explicit formulas were obtained for the electroosmotic velocity and streaming potential in a soft circular capillary. The research on different aspects of EOF in soft channels was continued in the subsequent years using different theoretical methods [13–17].

The research conducted in recent years on electrokinetic properties of PEL-coated channels is quite diverse. In a series of papers published by Werner and co-workers [8,18,19], detailed theoretical studies were conducted on electrokinetics of soft interfaces with single- and multilayered PELs that, unlike the vast majority of the available literature, were validated experimentally. Qian and his co-workers [20–22] studied different aspects of soft electrokinetics including EDL overlap and the field-effect regulation of the Donnan potential. More recently, the alternating current EOF of viscoelastic fluids was analytically studied by Li *et al.* [23]. Furthermore, lattice-Boltzmann simulations of EOF in coated capillaries were carried out by Melchionna and co-workers [24,25]. While the studies mentioned above all deal with simple geometries like circular or slit channels, more complex geometries such as conical [26] and rectangular [7,27] channels have been recently considered as well.

In all of the available research works concerning EOF in soft microchannels, it has been assumed that there is no difference between the tendencies of ions to accumulate inside or outside the PEL. This is true when the density of the grafted brushes is low so that the same dielectric permittivities are found in the bulk and in the PEL. However, since the permittivity of polyelectrolyte brushes is lower than that of the electrolyte, the effective permittivity of the PEL will be significantly smaller than that of the electrolyte for high grafting densities [28]. Under such circumstances, the ions will prefer to stay in the electrolyte, which is the medium of higher permittivity, leading to significant changes in the ionic distribution [29]. Such a phenomenon is called ion partitioning. Besides the partitioning of ions, another issue that needs to be taken into account for high grafting densities is the increase in the fluid viscosity in the PEL due to effects such as hydration [30,31]. It appears as if the difference between the dynamic viscosities within and outside the PEL has

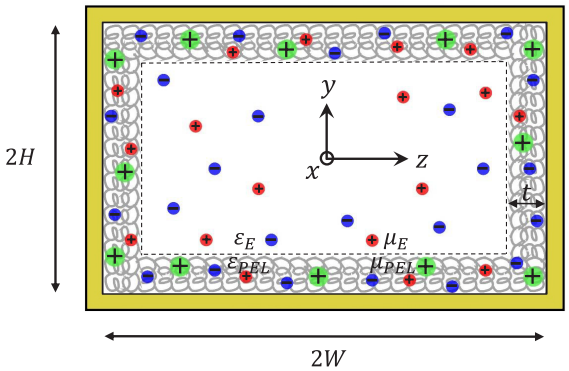

FIG. 1. Schematic of the soft microchannel under consideration including the dimensions and the coordinate system. The polyelectrolyte layer (PEL) is the region between the rigid wall and the dashed lines. It contains fixed ions, shown as large circles, whereas the electrolyte ions, represented by small circles, are mobile. Different physical properties are considered inside and outside the PEL.

not been considered so far when computing the EOF. These gaps are closed in this study by considering different permittivity and dynamic viscosity values inside and outside the PEL. The flow is considered to be both steady and fully developed, and the channel is assumed to be of a rectangular cross-sectional area, which is the shape commonly created by standard microfabrication methods [32]. The main approach adopted is a variational formulation of the linearized problem. In addition, numerical simulations of the nonlinear governing equations are performed utilizing a finite-element discretization. The variational formulation treats the whole fluid domain as a single medium with variable properties. The solutions are obtained using a spectral method. For the special case of a slit geometry, which is a representative of a rectangular channel when the aspect ratio is high, closed-form solutions in terms of basic functions are obtained. The importance of our work not only lies in incorporating the ion partitioning and hydration effects, but also in presenting formulations that can easily be applied to multidomain problems. This is crucial for modeling of PEL-covered channels having cross-sectional geometries other than circular or slitlike, where the classical approach of obtaining different solutions for inside and outside of the PEL followed by matching the solutions cannot be applied.

II. PROBLEM FORMULATION

A. Problem definition

The electrostatic potential, ionic concentration, and EOF in a rectangular microchannel with a PEL attached to the wall (shown schematically in Fig. 1), are studied in a steady-state configuration. The thickness of the PEL t is constant, and its fixed charges are uniformly distributed. The flow is assumed to be hydrodynamically fully developed and the physicochemical properties are considered to be constant. It is, however, assumed that the dielectric permittivity and the liquid viscosity are different inside and outside the PEL in order to obtain solutions valid at high PEL densities. In addition, the liquid is considered to contain a fully dissociated and symmetric electrolyte. While the number density of the fixed-charge groups are considered to be low when treating the problem analytically, no restriction is imposed when solving the governing equations numerically. Since there is symmetry with respect to both y and z axes, only a quarter of the channel is considered in the analysis.

B. Electric potential distribution

An understanding of the ionic distribution is necessary for the evaluation of the volumetric body force, which is required for obtaining the electroosmotic velocity. The distribution of ions is dictated by the electric potential distribution. The total electric potential φ within the channel is given by the

superposition of the externally applied electric potential Φ and that created due to the presence of the dissolved ions and fixed-charge groups. The former depends on x only, whereas the latter may be considered as a function of y and z. Hence, one may write

$$\varphi(x, y, z) = \Phi(x) + \psi(y, z). \tag{1}$$

The physical law governing the electric potential distribution is the Poisson equation, which relates φ to the net electric charge density ρ_e as

$$\nabla \cdot (\varepsilon \nabla \varphi) = -\rho_e, \tag{2}$$

where ε stands for the dielectric permittivity. For evaluation of the net electric charge in the channel, attention should be given to the fact that there are two types of electric charges in the channel: the dissolved ions, which can move freely throughout the channel, and the charges fixed to the PEL chains. As noted previously, partitioning of the dissolved ions occurs at the liquid/PEL interface, for example, because of differences in the electrostatic or van der Waals interaction energies of different types of ions. One well-known phenomenon is the difference in the electrostatic self-energies of the ions resulting from the permittivity difference, the so-called Born energy, to be considered below. The ratio of the ionic concentrations inside and outside the PEL is given by the partition coefficient P_i which, making use of the Boltzmann distribution, is given as [33]

$$P_i = \exp\left(-\frac{\Delta W_i}{k_B T}\right), \tag{3}$$

wherein k_B represents the Boltzmann constant, T stands for the absolute temperature, and ΔW_i is the energy difference of the ith ionic species. Assuming that ΔW_i is solely due to the Born energy and considering ions of spherical shape with radius r_i, it can be shown that [28]

$$\Delta W_i = \frac{e^2 \mathbb{Z}_E^2}{8\pi r_i}\left(\frac{1}{\varepsilon_{\mathrm{PEL}}} - \frac{1}{\varepsilon_E}\right). \tag{4}$$

Here, e is the proton charge, $\mathbb{Z}_E$ is the valency of the electrolyte ions, and ε_E and $\varepsilon_{\mathrm{PEL}}$ are the permittivities of the liquid and the PEL, respectively. Assuming the same radii for the anions and cations, that is, $r_- = r_+ = r$, which is roughly fulfilled for salts such as KCl [34], taking advantage of Eqs. (3) and (4), and adopting the Boltzmann distribution, the ionic concentration inside and outside the PEL is given as

$$c_\pm = c^\infty \exp\left(\mp \frac{e\mathbb{Z}_E \psi}{k_B T}\right) \exp\left[\frac{e^2 \mathbb{Z}_E^2}{8\pi r k_B T}\left(\frac{1}{\varepsilon_E} - \frac{1}{\varepsilon_{\mathrm{PEL}}}\right)\right], \tag{5}$$

$$c_\pm = c^\infty \exp\left(\mp \frac{e\mathbb{Z}_E \psi}{k_B T}\right), \tag{6}$$

where c^∞ stands for ionic concentration at neutral conditions. Instead of Eqs. (5) and (6), the following compact formula may be used to obtain the ionic concentration in both regions

$$c_\pm = c^\infty \exp\left(\mp \frac{e\mathbb{Z}_E \psi}{k_B T}\right) \exp\left[\frac{e^2 \mathbb{Z}_E^2}{8\pi r k_B T}\left(\frac{1}{\varepsilon_E} - \frac{1}{\varepsilon}\right)\right]. \tag{7}$$

Inside the PEL, where $\varepsilon = \varepsilon_{\mathrm{PEL}}$, Eq. (7) reduces to Eq. (5) and in the bulk electrolyte solution, for which $\varepsilon = \varepsilon_E$, Eq. (6) is recovered. Utilizing Eq. (7), the charge density of the electrolyte ions ρ_E is obtained as

$$\begin{aligned}\rho_E &= e\mathbb{Z}_E(c_+ - c_-) = e\mathbb{Z}_E c^\infty \left[\exp\left(-\frac{e\mathbb{Z}_E \psi}{k_B T}\right) - \exp\left(\frac{e\mathbb{Z}_E \psi}{k_B T}\right)\right] \exp\left[\frac{e^2 \mathbb{Z}_E^2}{8\pi r k_B T}\left(\frac{1}{\varepsilon_E} - \frac{1}{\varepsilon}\right)\right] \\ &= -2e\mathbb{Z}_E c^\infty \sinh\left(\frac{e\mathbb{Z}_E \psi}{k_B T}\right) \exp\left[\frac{e^2 \mathbb{Z}_E^2}{8\pi r k_B T}\left(\frac{1}{\varepsilon_E} - \frac{1}{\varepsilon}\right)\right].\end{aligned} \tag{8}$$

For evaluation of the volumetric charge density of the PEL fixed-charge groups ρ_{PEL}, a positive valence of $\mathbb{Z}_{\mathrm{PEL}}$ and a number density of $\mathbb{N}_{\mathrm{PEL}}$ are considered to yield

$$\rho_{\mathrm{PEL}} = e\mathbb{N}_{\mathrm{PEL}}\mathbb{Z}_{\mathrm{PEL}}. \tag{9}$$

Note that on the PEL chains charge regulation effects may occur, for example, Manning condensation [35,36]. Such effects imply a transfer of ions between the electrolyte solution and the PEL chains. In that context, Eq. (9) represents the effective charge density of the PEL molecules. Specifically, it is not assumed that the PEL chains are fully ionized. Because of potential changes in ion concentration due to charge regulation effects, the concentrations appearing in the model equations are the actual concentrations inside the channel. These may differ from the concentrations in the reservoirs to which the channel is connected.

Equation (8) may be substituted into Eq. (2) in order to obtain the equation governing the electric potential distribution in the PEL-free region, albeit with the consideration of Eq. (1) and the fact that Φ is a linear function of x. To obtain the corresponding equation for the PEL, the contribution of the fixed ions to the volumetric charge density should be accounted for from Eq. (9), i.e., $\rho_e = \rho_E + \rho_{\mathrm{PEL}}$. Since it is intended to perform a single analysis valid for both regions, it is not possible to use separate equations for inside and outside the PEL. Instead, the following compact form of the Poisson equation is used:

$$\frac{\partial}{\partial y}\left(\varepsilon\frac{\partial\psi}{\partial y}\right) + \frac{\partial}{\partial z}\left(\varepsilon\frac{\partial\psi}{\partial z}\right) - 2e\mathbb{Z}_E c^{\infty}\sinh\left(\frac{e\mathbb{Z}_E\psi}{k_BT}\right)\exp\left[\frac{e^2\mathbb{Z}_E^2}{8\pi r k_BT}\left(\frac{1}{\varepsilon_E}-\frac{1}{\varepsilon}\right)\right] + e\mathbb{N}\mathbb{Z}_{\mathrm{PEL}} = 0. \tag{10}$$

In Eq. (10), $\mathbb{N}$ denotes the density of the fixed charges and is 0 and $\mathbb{N}_{\mathrm{PEL}}$ outside and inside the PEL, respectively, thereby rendering Eq. (10) valid in both regions. Note that this equation is in fact valid for any cross-sectional distributions of ε and $\mathbb{N}$. Accordingly, although we finally apply the assumption of uniform PEL properties, the majority of the subsequent analysis is valid for PEL with position-dependent properties. In dimensionless form, Eq. (10) is written as

$$\frac{\partial}{\partial y^*}\left(\varepsilon^*\frac{\partial\psi^*}{\partial y^*}\right) + \frac{\partial}{\partial z^*}\left(\varepsilon^*\frac{\partial\psi^*}{\partial z^*}\right) - K^2\exp\left[\Xi\left(1-\frac{1}{\varepsilon^*}\right)\right]\sinh\psi^* + K^2\eta_\lambda^{-2}\mathbb{N}^* = 0, \tag{11}$$

in which $y^* = y/H$, $z^* = z/H$, $\varepsilon^* = \varepsilon/\varepsilon_E$, $\psi^* = e\mathbb{Z}_E\psi/k_BT$, $\mathbb{N}^* = \mathbb{N}/\mathbb{N}_{\mathrm{PEL}}$, and $\Xi = e^2\mathbb{Z}_E^2/8\pi r k_BT\varepsilon_E$. Furthermore, $K = H/\lambda_E$ with $\lambda_E = (k_BT\varepsilon_E/2e^2\mathbb{Z}_E^2c^{\infty})^{1/2}$ being the characteristic EDL thickness and $\eta_\lambda = \lambda_{\mathrm{PEL}}/\lambda_E$, with $\lambda_{\mathrm{PEL}} = (k_BT\varepsilon_E/\mathbb{Z}_E\mathbb{Z}_{\mathrm{PEL}}\mathbb{N}_{\mathrm{PEL}}e^2)^{1/2}$ representing an equivalent EDL thickness inside the PEL. Equation (11) is nonlinear and, hence, should generally be solved utilizing numerical tools. It is, however, possible to linearize this equation by approximating $\sinh\psi^*$ by ψ^* for small electric potentials, that is, for $\psi^* \leqslant 1$. This approximation, known as the Debye-Hückel linearization, results in

$$\frac{\partial}{\partial y^*}\left(\varepsilon^*\frac{\partial\psi^*}{\partial y^*}\right) + \frac{\partial}{\partial z^*}\left(\varepsilon^*\frac{\partial\psi^*}{\partial z^*}\right) - K^2\exp\left[\Xi\left(1-\frac{1}{\varepsilon^*}\right)\right]\psi^* + K^2\eta_\lambda^{-2}\mathbb{N}^* = 0. \tag{12}$$

Equation (12) needs to be solved considering the following boundary conditions:

$$\left.\frac{\partial\psi^*}{\partial y^*}\right|_{y^*=0} = \left.\frac{\partial\psi^*}{\partial z^*}\right|_{z^*=0} = \left.\frac{\partial\psi^*}{\partial y^*}\right|_{y^*=1} = \left.\frac{\partial\psi^*}{\partial z^*}\right|_{z^*=W^*} = 0, \tag{13}$$

wherein $W^* = W/H$ stands for the channel aspect ratio. The first two of the boundary conditions in Eq. (13) represent the symmetry at the centerlines, while the following two reflect the fact that the channel walls are considered uncharged. Note that the PEL/electrolyte interface is now an internal region and the interfacial conditions therein are automatically satisfied by the formulation. We utilize the variational calculus for solving Eq. (12) subject to the boundary conditions (13). In this technique, instead of directly solving Eq. (12), the solution is obtained by the minimization of the

following functional [37]:

$$I_\psi = \int_{\mathbb{A}^*} \left\{ \varepsilon^* \left(\frac{\partial \psi^*}{\partial y^*} \right)^2 + \varepsilon^* \left(\frac{\partial \psi^*}{\partial z^*} \right)^2 + K^2 \exp\left[\Xi \left(1 - \frac{1}{\varepsilon^*} \right) \right] \psi^{*2} - 2K^2 \eta_\lambda^{-2} \mathbb{N}^* \psi^* \right\} d\mathbb{A}^*. \quad (14)$$

Note that $I_\psi = \int_{\mathbb{A}^*} \mathbb{F} d\mathbb{A}^*$ is constructed so that

$$\frac{\partial \mathbb{F}}{\partial \psi^*} - \frac{\partial (\partial \mathbb{F} / \partial \psi^*_{y^*})}{\partial y^*} - \frac{\partial (\partial \mathbb{F} / \partial \psi^*_{z^*})}{\partial z^*} = 0 \quad (15)$$

reduces to Eq. (12) [38]. In Eq. (15), the subscripts y^* and z^* represent partial differentiation with respect to these variables. The transformation of the differential equation into an integral over the dimensionless area $\mathbb{A}^* = \mathbb{A}/H^2$ by means of the variational calculus is the key to bypassing the difficulties pertinent to matching different solutions valid in different domains. In the following, ψ^* is expanded in terms of a complete and linearly independent set of basis functions f_j, that is,

$$\psi^* = \sum_{j=1}^{M} b_j f_j. \quad (16)$$

One is allowed to select any type of basis functions provided the boundary conditions (13) are satisfied without imposing unphysical constraints on the solution. Given the ease of utilizing the trigonometric functions, f_j is written as

$$f_j(y^*, z^*) = \cos(\xi_{l_j} y^*) \cos\left(\frac{\xi_{m_j} z^*}{W^*} \right), \quad (17)$$

where $\xi_{l_j} = l_j \pi$ and $\xi_{m_j} = m_j \pi$ with $l_j = 0,\ 1,\ 2,\ \ldots, l_{\max}$ and $m_j = 0,\ 1,\ 2,\ \ldots, m_{\max}$. Note that l_j and m_j are varied independently to provide a complete set of the basis functions and, hence, the number of the basis functions becomes $M = (l_{\max} + 1)(m_{\max} + 1)$. Since I_ψ is a function of $b_1, b_2, \ldots,\ b_M$, its minimization requires having

$$\frac{\partial I_\psi}{\partial b_i} = 0 \quad \text{for } i = 1,\ 2,\ \ldots,\ M, \quad (18)$$

which leads to

$$\sum_{j=1}^{M} b_j \int_{\mathbb{A}^*} \left\{ \varepsilon^* \frac{\partial f_i}{\partial y^*} \frac{\partial f_j}{\partial y^*} + \varepsilon^* \frac{\partial f_i}{\partial z^*} \frac{\partial f_j}{\partial z^*} + K^2 \exp\left[\Xi \left(1 - \frac{1}{\varepsilon^*} \right) \right] f_i f_j \right\} d\mathbb{A}^*$$

$$= K^2 \eta_\lambda^{-2} \int_{\mathbb{A}^*} \mathbb{N}^* f_i d\mathbb{A}^* \quad \text{for } i = 1,\ 2,\ \ldots,\ M. \quad (19)$$

Equation (19) represents a system of M equations for the M unknowns b_1 to b_M. The matrix form of this equation can be expressed as

$$\mathbf{A}\mathbf{b} = \mathbf{C}, \quad (20)$$

wherein the symmetric matrix $\mathbf{A}$ and vector $\mathbf{C}$ possess the following elements:

$$a_{ij} = \int_{\mathbb{A}^*} \left\{ \varepsilon^* \frac{\partial f_i}{\partial y^*} \frac{\partial f_j}{\partial y^*} + \varepsilon^* \frac{\partial f_i}{\partial z^*} \frac{\partial f_j}{\partial z^*} + K^2 \exp\left[\Xi \left(1 - \frac{1}{\varepsilon^*} \right) \right] f_i f_j \right\} d\mathbb{A}^*, \quad (21)$$

$$c_i = K^2 \eta_\lambda^{-2} \int_{\mathbb{A}^*} \mathbb{N}^* f_i d\mathbb{A}^*. \quad (22)$$

The vector $\mathbf{b}$ stands for the coefficients $b_1, b_2, \ldots,\ b_M$. Effectively, the outlined approach constitutes a spectral method. For the determination of $\mathbf{A}$ and $\mathbf{C}$ utilizing Eqs. (21) and (22), we apply the assumption of constant PEL properties. The corresponding expressions can be found in Appendix A. The linear algebraic system Eq. (20) can be solved by applying common numerical methods.

C. Velocity distribution

The momentum conservation in the microchannel is governed by the Navier-Stokes equations. For a steady and hydrodynamically fully developed flow, only the axial momentum equation matters, which is given as

$$\frac{\partial}{\partial y}\left(\mu\frac{\partial u}{\partial y}\right)+\frac{\partial}{\partial z}\left(\mu\frac{\partial u}{\partial z}\right)-\frac{\partial p}{\partial x}+F=0. \tag{23}$$

In Eq. (23), u is the axial velocity, p represents the pressure, F stands for the body force in the axial direction, and μ denotes the dynamic viscosity, which is allowed to vary over the channel cross-sectional area. There are two body forces in the problem under consideration which are the electroosmotic force and the resistive force created by the polyelectrolyte layer. The former is created upon the interaction of the electric field and the electrolyte ions and is given as $\rho_E E_x$, with $E_x=-d\Phi/dx$ being the externally applied electric field. The volumetric resistive force of the PE layer is usually considered to be proportional to the velocity and, for a fully developed flow, is given as $\mathbb{f}_{\mathrm{PEL}}u$ where $\mathbb{f}_{\mathrm{PEL}}$ denotes the friction coefficient inside the PEL per unit volume [3]. Considering the two contributions to the body force in Eq. (23), after substitution for ρ_E from Eq. (8), and omitting the pressure gradient for a purely electroosmotic flow, the compact form of the momentum equation is

$$\frac{\partial}{\partial y}\left(\mu\frac{\partial u}{\partial y}\right)+\frac{\partial}{\partial z}\left(\mu\frac{\partial u}{\partial z}\right)-\mathbb{f}u-2e\,\mathbb{z}_E c^{\infty}E_x\sinh\left(\frac{e\,\mathbb{z}_E\psi}{k_BT}\right)\exp\left[\frac{e^2\mathbb{z}_E^2}{8\pi r k_BT}\left(\frac{1}{\varepsilon_E}-\frac{1}{\varepsilon}\right)\right]=0, \tag{24}$$

wherein $\mathbb{f}$ represents the friction coefficient, which is $\mathbb{f}_{\mathrm{PEL}}$ and 0 inside and outside the PEL, respectively. Introducing four new dimensionless parameters, $u^*=-e\mathbb{Z}_E\mu_E u/\varepsilon_E k_BTE_x$ (with μ_E denoting the dynamic viscosity of the bulk electrolyte solution), $\mu^*=\mu/\mu_E$, $\mathbb{f}^*=\mathbb{f}/\mathbb{f}_{\mathrm{PEL}}$, and $\alpha=H(\mathbb{f}_{\mathrm{PEL}}/\mu_E)^{1/2}$, the momentum equation (24) is rewritten as

$$\frac{\partial}{\partial y^*}\left(\mu^*\frac{\partial u^*}{\partial y^*}\right)+\frac{\partial}{\partial z^*}\left(\mu^*\frac{\partial u^*}{\partial z^*}\right)-\alpha^2\mathbb{f}^*u^*+K^2\exp\left[\Xi\left(1-\frac{1}{\varepsilon^*}\right)\right]\sinh\psi^*=0, \tag{25}$$

which, upon application of the Debye-Hückel linearization, reduces to

$$\frac{\partial}{\partial y^*}\left(\mu^*\frac{\partial u^*}{\partial y^*}\right)+\frac{\partial}{\partial z^*}\left(\mu^*\frac{\partial u^*}{\partial z^*}\right)-\alpha^2\mathbb{f}^*u^*+K^2\exp\left[\Xi\left(1-\frac{1}{\varepsilon^*}\right)\right]\psi^*=0. \tag{26}$$

The dimensionless momentum equation is subject to symmetry and no-slip boundary conditions, given as

$$\left.\frac{\partial u^*}{\partial y^*}\right|_{y^*=0}=\left.\frac{\partial u^*}{\partial z^*}\right|_{z^*=0}=u^*|_{y^*=1}=u^*|_{z^*=W^*}=0. \tag{27}$$

The momentum equation can be derived from minimization of the following functional:

$$I_u=\int_{\mathbb{A}^*}\left\{\mu^*\left(\frac{\partial u^*}{\partial y^*}\right)^2+\mu^*\left(\frac{\partial u^*}{\partial z^*}\right)^2+\alpha^2\mathbb{f}^*u^{*2}-2K^2\exp\left[\Xi\left(1-\frac{1}{\varepsilon^*}\right)\right]\psi^*u^*\right\}d\mathbb{A}^*. \tag{28}$$

We now consider u^* of the form

$$u^*=\sum_{j=1}^{N}d_jg_j, \tag{29}$$

wherein the basis functions are

$$g_j=\cos(\xi_{r_j}y^*)\cos\left(\frac{\xi_{q_j}z^*}{W^*}\right), \tag{30}$$

where $\xi_{r_j} = (2r_j + 1)\pi/2$ and $\xi_{q_j} = (2q_j + 1)\pi/2$, with $r_j = 0,\ 1,\ 2,\ \ldots, r_{\max}$ and $q_j = 0,\ 1,\ 2,\ \ldots, q_{\max}$. The number of basis functions, therefore, becomes $N = (r_{\max} + 1)(q_{\max} + 1)$. The minimization of $I_u(d_1, d_2, \ldots,\ d_N)$ requires having

$$\frac{\partial I_u}{\partial d_i} = 0 \quad \text{for } i = 1,\ 2,\ \ldots,\ N. \tag{31}$$

Differentiating Eq. (28) with respect to d_i results in

$$\int_{\mathbb{A}^*} \left\{ \mu^* \frac{\partial u^*}{\partial y^*} \frac{\partial g_i}{\partial y^*} + \mu^* \frac{\partial u^*}{\partial z^*} \frac{\partial g_i}{\partial z^*} + \alpha^2 \mathbb{f}^* u^* g_i - K^2 \exp\left[\Xi \left(1 - \frac{1}{\varepsilon^*} \right) \right] \psi^* g_i \right\} d\mathbb{A}^* = 0 \quad \text{for } i = 1,\ 2,\ \ldots,\ N. \tag{32}$$

After the introduction of u^* from Eq. (29) into Eq. (32), it becomes

$$\sum_{j=1}^{N} d_j \int_{\mathbb{A}^*} \left(\mu^* \frac{\partial g_i}{\partial y^*} \frac{\partial g_j}{\partial y^*} + \mu^* \frac{\partial g_i}{\partial z^*} \frac{\partial g_j}{\partial z^*} + \alpha^2 \mathbb{f}^* g_i g_j \right) d\mathbb{A}^* = K^2 \int_{\mathbb{A}^*} \exp\left[\Xi \left(1 - \frac{1}{\varepsilon^*} \right) \right] \psi^* g_i d\mathbb{A}^* \quad \text{for } i = 1,\ 2,\ \ldots,\ N. \tag{33}$$

which is a system of N equations for N unknowns, written in matrix form as

$$\mathbf{Ed} = \mathbf{H}, \tag{34}$$

wherein the matrix $\mathbf{E}$ and vector $\mathbf{H}$ are composed of the following elements:

$$e_{ij} = \int_{\mathbb{A}^*} \left(\mu^* \frac{\partial g_i}{\partial y^*} \frac{\partial g_j}{\partial y^*} + \mu^* \frac{\partial g_i}{\partial z^*} \frac{\partial g_j}{\partial z^*} + \alpha^2 \mathbb{f}^* g_i g_j \right) d\mathbb{A}^*, \tag{35}$$

$$h_i = K^2 \int_{\mathbb{A}^*} \exp\left[\Xi \left(1 - \frac{1}{\varepsilon^*} \right) \right] \psi^* g_i d\mathbb{A}^*. \tag{36}$$

The vector $\mathbf{d}$ stands for the coefficients $d_1, d_2, \ldots,\ d_N$. Again, we apply the assumption of constant PEL properties. The corresponding expressions for e_{ij} and h_i can be found in Appendix B. The linear algebraic system Eq. (34) can be solved by applying common numerical methods.

Having computed the solution, the parameters of physical interest such as the mean velocity can be obtained. The mean velocity in dimensionless form is given as

$$u_m^* = \frac{\int_0^{W^*} \int_0^1 u^* dy^* dz^*}{\int_0^{W^*} \int_0^1 dy^* dz^*} = \sum_{j=1}^{N} \frac{d_j (-1)^{r_j + q_j}}{\xi_{r_j} \xi_{q_j}}. \tag{37}$$

D. Special solution for $1 \ll W^*$

When the width of the channel is significantly larger than the height, that is, when $1 \ll W^*$, the problem is significantly simplified since the z dependence of the electric potential and fluid velocity disappears except for vanishingly small regions near the vertical walls. Neglecting these regions, the electric potential and momentum equations are reduced to ordinary differential equations that are easy to be solved via the classical approach of obtaining separate solutions for the core and the PEL, after which the solutions are matched. Discarding the derivative with respect to z in Eq. (12), it reduces to Eqs. (38) and (39) outside and inside the PEL, respectively:

$$\frac{d^2 \psi_E^*}{dy^{*2}} - K^2 \psi_E^* = 0, \tag{38}$$

$$\eta_\varepsilon \frac{d^2 \psi_{\text{PEL}}^*}{dy^{*2}} - K^2 \exp\left[\Xi \left(1 - \eta_\varepsilon^{-1} \right) \right] \psi_{\text{PEL}}^* + K^2 \eta_\lambda^{-2} = 0, \tag{39}$$

which are subject to the following interfacial and boundary conditions:

$$\left.\frac{d\psi_E^*}{dy^*}\right|_{y^*=0} = \left.\frac{d\psi_{\mathrm{PEL}}^*}{dy^*}\right|_{y^*=1} = 0,\ \ \psi_E^*|_{y^*=1-t^*} = \psi_{\mathrm{PEL}}^*|_{y^*=1-t^*},\ \ \left.\frac{d\psi_E^*}{dy^*}\right|_{y^*=1-t^*} = \eta_\varepsilon \left.\frac{d\psi_{\mathrm{PEL}}^*}{dy^*}\right|_{y^*=1-t^*}. \tag{40}$$

It can be shown that the solutions of Eqs. (38) and (39) subject to the boundary conditions (40) are given as

$$\psi_E^* = A_1 \cosh(Ky^*), \tag{41}$$

$$\psi_{\mathrm{PEL}}^* = B_1\left[\cosh\left(K\gamma^{1/2}\eta_\varepsilon^{-1/2}y^*\right) - \tanh\left(K\gamma^{1/2}\eta_\varepsilon^{-1/2}\right)\sinh\left(K\gamma^{1/2}\eta_\varepsilon^{-1/2}y^*\right)\right] + \eta_\lambda^{-2}\gamma^{-1}, \tag{42}$$

wherein $\gamma = \exp[\Xi(1-\eta_\varepsilon^{-1})]$ and the coefficients A_1 and B_1 are given as

$$\begin{aligned} A_1 = {} & \eta_\lambda^{-2}\gamma^{-1/2}\eta_\varepsilon^{1/2}\{\sinh[K(1-t^*)]\}^{-1}\left\{\tanh\left[K\gamma^{1/2}\eta_\varepsilon^{-1/2}(1-t^*)\right] - \tanh\left(K\gamma^{1/2}\eta_\varepsilon^{-1/2}\right)\right\} \\ & \times \Big[(\gamma\eta_\varepsilon)^{1/2}\{\tanh[K(1-t^*)]\}^{-1}\left\{\tanh\left[K\gamma^{1/2}\eta_\varepsilon^{-1/2}(1-t^*)\right] - \tanh\left(K\gamma^{1/2}\eta_\varepsilon^{-1/2}\right)\right\} \\ & - 1 + \tanh\left(K\gamma^{1/2}\eta_\varepsilon^{-1/2}\right)\tanh\left[K\gamma^{1/2}\eta_\varepsilon^{-1/2}(1-t^*)\right]\Big]^{-1}, \end{aligned} \tag{43}$$

$$\begin{aligned} B_1 = {} & \eta_\lambda^{-2}\gamma^{-1}\left\{\cosh\left[K\gamma^{1/2}\eta_\varepsilon^{-1/2}(1-t^*)\right]\right\}^{-1}\Big[(\gamma\eta_\varepsilon)^{1/2}\{\tanh[K(1-t^*)]\}^{-1} \\ & \times\left\{\tanh\left[K\gamma^{1/2}\eta_\varepsilon^{-1/2}(1-t^*)\right] - \tanh\left(K\gamma^{1/2}\eta_\varepsilon^{-1/2}\right)\right\} - 1 + \tanh\left(K\gamma^{1/2}\eta_\varepsilon^{-1/2}\right) \\ & \times\tanh\left[K\gamma^{1/2}\eta_\varepsilon^{-1/2}(1-t^*)\right]\Big]^{-1} \end{aligned} \tag{44}$$

In the same way, from Eq. (26), the dimensionless momentum equations for the bulk and the PEL are obtained as

$$\frac{d^2u_E^*}{dy^{*2}} + K^2\psi_E^* = 0, \tag{45}$$

$$\eta_\mu\frac{d^2u_{\mathrm{PEL}}^*}{dy^{*2}} - \alpha^2u_{\mathrm{PEL}}^* + K^2\gamma\psi_{\mathrm{PEL}}^* = 0. \tag{46}$$

Equations (45) and (46) should satisfy the following boundary conditions:

$$\left.\frac{du_E^*}{dy^*}\right|_{y^*=0} = u_{\mathrm{PEL}}^*|_{y^*=1} = 0,\ \ u_E^*|_{y^*=1-t^*} = u_{\mathrm{PEL}}^*|_{y^*=1-t^*},\ \ \left.\frac{du_E^*}{dy^*}\right|_{y^*=1-t^*} = \eta_\mu\left.\frac{du_{\mathrm{PEL}}^*}{dy^*}\right|_{y^*=1-t^*}. \tag{47}$$

It is easy to verify that the solutions of Eqs. (45) and (46) fulfilling the boundary conditions are given as

$$u_E^* = -A_1\cosh(Ky^*) + A_2, \tag{48}$$

$$\begin{aligned} u_{\mathrm{PEL}}^* = {} & B_2\left[\cosh\left(\alpha\eta_\mu^{-1/2}y^*\right) - \coth\left(\alpha\eta_\mu^{-1/2}\right)\sinh\left(\alpha\eta_\mu^{-1/2}y^*\right)\right] \\ & + \left\{\left[\cosh\left(K\gamma^{1/2}\eta_\varepsilon^{-1/2}\right)\right]^{-1}\left(\frac{K^2\gamma\eta_\varepsilon B_1}{K^2\gamma\eta_\mu - \alpha^2\eta_\varepsilon}\right) - \frac{K^2}{\alpha^2\eta_\lambda^2}\right\}\frac{\sinh\left(\alpha\eta_\mu^{-1/2}y^*\right)}{\sinh\left(\alpha\eta_\mu^{-1/2}\right)} \\ & - \left(\frac{K^2\gamma\eta_\varepsilon B_1}{K^2\gamma\eta_\mu - \alpha^2\eta_\varepsilon}\right)\cosh\left(K\gamma^{1/2}\eta_\varepsilon^{-1/2}y^*\right) \\ & + \tanh\left(K\gamma^{1/2}\eta_\varepsilon^{-1/2}\right)\left(\frac{K^2\gamma\eta_\varepsilon B_1}{K^2\gamma\eta_\mu - \alpha^2\eta_\varepsilon}\right)\sinh\left(K\gamma^{1/2}\eta_\varepsilon^{-1/2}y^*\right) + \frac{K^2}{\alpha^2\eta_\lambda^2}, \end{aligned} \tag{49}$$

with the following coefficients:

$$A_2 = B_2\{\cosh[\alpha\eta_\mu^{-1/2}(1-t^*)] - \coth(\alpha\eta_\mu^{-1/2})\sinh[\alpha\eta_\mu^{-1/2}(1-t^*)]\}$$
$$+\left\{[\cosh(K\gamma^{1/2}\eta_\varepsilon^{-1/2})]^{-1}\left(\frac{K^2\gamma\eta_\varepsilon B_1}{K^2\gamma\eta_\mu-\alpha^2\eta_\varepsilon}\right)-\frac{K^2}{\alpha^2\eta_\lambda^2}\right\}\frac{\sinh[\alpha\eta_\mu^{-1/2}(1-t^*)]}{\sinh(\alpha\eta_\mu^{-1/2})}$$
$$-\left(\frac{K^2\gamma\eta_\varepsilon B_1}{K^2\gamma\eta_\mu-\alpha^2\eta_\varepsilon}\right)\cosh[K\gamma^{1/2}\eta_\varepsilon^{-1/2}(1-t^*)]+\tanh(K\gamma^{1/2}\eta_\varepsilon^{-1/2})\left(\frac{K^2\gamma\eta_\varepsilon B_1}{K^2\gamma\eta_\mu-\alpha^2\eta_\varepsilon}\right)$$
$$\times\sinh[K\gamma^{1/2}\eta_\varepsilon^{-1/2}(1-t^*)]+\frac{K^2}{\alpha^2\eta_\lambda^2}+A_1\cosh[K(1-t^*)], \tag{50}$$

$$B_2 = \alpha^{-1}\eta_\mu^{-1/2}\{\sinh[\alpha\eta_\mu^{-1/2}(1-t^*)] - \coth(\alpha\eta_\mu^{-1/2})\cosh[\alpha\eta_\mu^{-1/2}(1-t^*)]\}^{-1}$$
$$\times\Big[\Big[-A_1K\sinh[K(1-t^*)]-\alpha\eta_\mu^{1/2}\left\{[\cosh(K\gamma^{1/2}\eta_\varepsilon^{-1/2})]^{-1}\left(\frac{K^2\gamma\eta_\varepsilon B_1}{K^2\gamma\eta_\mu-\alpha^2\eta_\varepsilon}\right)-\frac{K^2}{\alpha^2\eta_\lambda^2}\right\}$$
$$\times\frac{\cosh[\alpha\eta_\mu^{-1/2}(1-t^*)]}{\sinh(\alpha\eta_\mu^{-1/2})}+\left(\frac{\eta_\mu K^3\gamma^{3/2}\eta_\varepsilon^{1/2}B_1}{K^2\gamma\eta_\mu-\alpha^2\eta_\varepsilon}\right)\sinh[K\gamma^{1/2}\eta_\varepsilon^{-1/2}(1-t^*)]$$
$$-\left(\frac{\eta_\mu K^3\gamma^{3/2}\eta_\varepsilon^{1/2}B_1}{K^2\gamma\eta_\mu-\alpha^2\eta_\varepsilon}\right)\tanh(K\gamma^{1/2}\eta_\varepsilon^{-1/2})\cosh[K\gamma^{1/2}\eta_\varepsilon^{-1/2}(1-t^*)]\Big]\Big]. \tag{51}$$

The dimensionless mean velocity becomes

$$u_m^* = \int_0^{1-t^*} u_E^* dy^* + \int_{1-t^*}^1 u_{\mathrm{PEL}}^* dy^*$$
$$= -\frac{A_1}{\mathrm{K}}\sinh[K(1-t^*)] + A_2(1-t^*) - \alpha^{-1}\eta_\mu^{1/2}B_2$$
$$\times\{\sinh[\alpha\eta_\mu^{-1/2}(1-t^*)] - \coth(\alpha\eta_\mu^{-1/2})\cosh[\alpha\eta_\mu^{-1/2}(1-t^*)] + [\sinh(\alpha\eta_\mu^{-1/2})]^{-1}\}$$
$$+\alpha^{-1}\eta_\mu^{1/2}\left\{[\cosh(K\gamma^{1/2}\eta_\varepsilon^{-1/2})]^{-1}\left(\frac{K^2\gamma\eta_\varepsilon B_1}{K^2\gamma\eta_\mu-\alpha^2\eta_\varepsilon}\right)-\frac{K^2}{\alpha^2\eta_\lambda^2}\right\}$$
$$\times\left\{\coth(\alpha\eta_\mu^{-1/2})-\frac{\cosh[\alpha\eta_\mu^{-1/2}(1-t^*)]}{\sinh(\alpha\eta_\mu^{-1/2})}\right\}-\left(\frac{K\gamma^{1/2}\eta_\varepsilon^{3/2}B_1}{K^2\gamma\eta_\mu-\alpha^2\eta_\varepsilon}\right)\{\sinh(K\gamma^{1/2}\eta_\varepsilon^{-1/2})$$
$$-\sinh[K\gamma^{1/2}\eta_\varepsilon^{-1/2}(1-t^*)]\}+\tanh(K\gamma^{1/2}\eta_\varepsilon^{-1/2})\left(\frac{K\gamma^{1/2}\eta_\varepsilon^{3/2}B_1}{K^2\gamma\eta_\mu-\alpha^2\eta_\varepsilon}\right)$$
$$\times\{\cosh(K\gamma^{1/2}\eta_\varepsilon^{-1/2})-\cosh[K\gamma^{1/2}\eta_\varepsilon^{-1/2}(1-t^*)]\}+\frac{K^2t^*}{\alpha^2\eta_\lambda^2}. \tag{52}$$

E. Incorporating the wall charge effects

Consistent with the recent literature, the channel wall was assumed neutral in the preceding analysis to reduce the number of the governing parameters. Although the presentation of the results also relies on this assumption, the modifications required for incorporating the wall charge effects into the model are briefly discussed here, since in realistic systems the wall charge may become important. In the presence of a nonzero surface charge density σ, the wall boundary conditions in Eq. (13) transform into

$$\left.\frac{\partial\psi^*}{\partial y^*}\right|_{y^*=1} = \left.\frac{\partial\psi^*}{\partial z^*}\right|_{z^*=W^*} = \sigma^*, \tag{53}$$

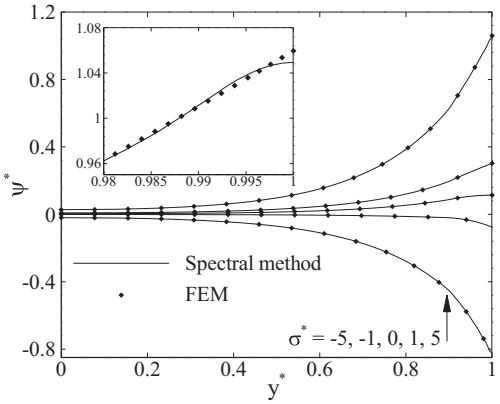

FIG. 2. Profiles of ψ^* at the vertical centerline for different values of σ^*, while keeping $W^* = 1$, $t^* = 0.1$, $K = 5$, $\eta_\lambda = 2$, $\Xi = 1.078$, and $\eta_\varepsilon = 0.8$. The results of the spectral method obtained utilizing $l_{\max} = m_{\max} = 100$ are compared with the predictions of the FEM-based numerical solution of Eq. (12). The inset shows the results for $\sigma^* = 5$.

where $\sigma^* = e\mathbb{Z}_E H\sigma/k_B T\varepsilon_{\mathrm{PEL}}$. According to Rektorys [37], the functional I_ψ is modified for this case by the inclusion of two line integrals at the walls, that is,

$$I_\psi = \int_{\mathbb{A}^*} \left\{ \varepsilon^* \left(\frac{\partial \psi^*}{\partial y^*} \right)^2 + \varepsilon^* \left(\frac{\partial \psi^*}{\partial z^*} \right)^2 + K^2 \exp\left[\Xi \left(1 - \frac{1}{\varepsilon^*} \right) \right] \psi^{*2} - 2K^2 \eta_\lambda^{-2} \mathbb{N}^* \psi^* \right\} d\mathbb{A}^*$$
$$- 2 \int_0^1 (\sigma^* \varepsilon^* \psi^*)_{z^*=W^*} dy^* - 2 \int_0^{W^*} (\sigma^* \varepsilon^* \psi^*)_{y^*=1} dz^*. \tag{54}$$

The addition of the line integrals to the functional does not affect the matrix $\mathbf{A}$ but modifies the elements of the vector $\mathbf{C}$ according to

$$c_i = K^2 \eta_\lambda^{-2} \int_{\mathbb{A}^*} \mathbb{N}^* f_i d\mathbb{A}^* + \int_0^1 (\sigma^* \varepsilon^* f_i)_{z^*=W^*} dy^* + \int_0^{W^*} (\sigma^* \varepsilon^* f_i)_{y^*=1} dz^*. \tag{55}$$

In principle, the basis functions f_i in the presence of a surface charge density should impose no constraint on the value of the electric potential gradient at the wall. This means that, in a strict sense, the basis functions used in Sec. II B are not appropriate for this case. Nevertheless, as will be shown below, these basis functions can provide sufficiently accurate results. Adopting the basis functions given by Eq. (17) and performing the integrations in Eq. (55) for a uniform σ^*, the elements c_i are obtained as

$$c_i = K^2 \eta_\lambda^{-2} W^* \left[\left[\delta_{0,l_i+m_i} - \left\{ \delta_{0,l_i}(1 - t^*) + \left(1 - \delta_{0,l_i}\right) \frac{\sin\left[\xi_{l_i}(1 - t^*)\right]}{\xi_{l_i} + \delta_{0,l_i}} \right\} \right.\right.$$
$$\left.\left. \times \left\{ \delta_{0,m_i}(1 - t^*/W^*) + \left(1 - \delta_{0,m_i}\right) \frac{\sin\left[\xi_{m_i}(1 - t^*/W^*)\right]}{\xi_{m_i} + \delta_{0,m_i}} \right\} \right]$$
$$+ \sigma^* \eta_\varepsilon \left[\delta_{0,l_i} (-1)^{m_i} + \delta_{0,m_i} W^* (-1)^{l_i} \right]. \tag{56}$$

To assess the accuracy of the solution developed for a charged wall in the space of cosine functions, in Fig. 2 the computed values of ψ^* at the vertical centerline are compared with finite-element-(FEM) based results for different values of σ^*. The corresponding numerical scheme is described in Sec. II F. Different from the other FEM-based results reported in this work, the Debye-Hückel linearization was applied for this purpose to restrict the errors solely to those occurring due to the

TABLE I. List of the dimensionless groups governing the physical problem under consideration.

Parameter	Definition
Channel aspect ratio W^*	W/H
Dimensionless PEL thickness t^*	t/H
Dimensionless Debye-Hückel parameter K	H/λ_E
EDL thickness ratio η_λ	$\lambda_{\mathrm{PEL}}/\lambda_E$
Partitioning parameter Ξ	$e^2\mathbb{z}_E^2/8\pi rk_BT\varepsilon_E$
Permittivity ratio η_ε	$\varepsilon_{\mathrm{PEL}}/\varepsilon_E$
Viscosity ratio η_μ	μ_{PEL}/μ_E
Dimensionless friction coefficient α	$H(\mathbb{f}_{\mathrm{PEL}}/\mu_E)^{1/2}$

choice of basis functions (17). It can be seen that there is a good agreement between both sets of results. The effect of the zero-gradient constraint imposed by the basis functions is not observed in the main figure but is only visible in the inset, which shows that the region over which there is a noticeable discrepancy between both sets of results is limited to the utmost vicinity of the wall. This region may be narrowed down to any desired extent by increasing the number of basis functions. Therefore, the conclusion is that the variational formulation allows obtaining accurate results for the electric potential in the presence of wall charges even in a space of functions that is not compatible with the boundary condition at the wall.

F. Numerical solution of the nonlinear equations

One main assumption the analysis presented above is based on is the validity of the Debye-Hückel linearization. To check the validity of this assumption, the nonlinear governing equations including Eqs. (11) and (25) were solved subject to the boundary conditions (13) and (27) plus the interfacial conditions comprising the continuity of the electric potential, electric displacement, velocity, and shear stress, utilizing COMSOL MULTIPHYSICS version 5.2. Finite-element simulations were performed based on Lagrange shape functions of quadratic order. All the elements were of rectangular shape. Nonuniform mapped meshing was used to locate smaller elements close to the boundaries and corners. The exterior boundaries of each subdomain were divided into 200 parts. Overall, 16×10^4 elements were employed which was found to be enough for obtaining virtually mesh-independent results. The resulting nonlinear equations were solved iteratively using Newton's method. The iterations were continued until the maximum relative error over the solution domain became less than 10^{-9}.

III. RESULTS AND DISCUSSION

It was shown that eight dimensionless groups, i.e., W^*, t^*, K, η_λ, Ξ, η_ε, η_μ, and α govern the electroosmotic flow in rectangular microchannels with neutral walls covered with PELs. These dimensionless parameters are listed in Table I. In this section, their interactive effects on the electrostatic potential, ionic concentration, and the flow characteristics are discussed in detail. Since performing a complete parametric study in an eight-dimensional space is not possible with reasonable effort, we have to fix some of the parameters at reference values. Along this line, it is assumed that the effective ionic radius is 3.3×10^{-10} m, corresponding to KCl ions. Moreover, it is assumed that the working fluid is water at 20 °C with a permittivity of $\varepsilon_E = 80 \times 8.854 \times 10^{-12}$ C V^{-1} m^{-1}. Hence, given the values of 1.6×10^{-19} C and 1.38×10^{-23} J K^{-1} for e and k_B, respectively, Ξ becomes 1.078. In addition, unless otherwise stated, we set $\eta_\lambda = 1$ which means that the characteristic EDL thickness of the bulk liquid is the same as the EDL thickness of the PEL. Hence, the parametric study is performed utilizing only six dimensionless groups whose values are selected according to the typical ranges of the PEL properties, given in Table II. All of the results

TABLE II. Typical ranges of the PEL properties.

Parameter	Value	Reference
Thickness t	0.7–198 nm	[25,43]
Density of fixed charges divided by Avogadro's number $\mathbb{N}_{\mathrm{PEL}}/N_A$	0.4–200 mol m^{-3}	[43]
Square root of ratio of viscosity and friction coefficient $(\mu_{\mathrm{PEL}}/\mathbb{f}_{\mathrm{PEL}})^{1/2}$	0.059–55 nm	[43]
Relative permittivity $\varepsilon_{\mathrm{PEL}}/\varepsilon_0$	52.8–78	[44,45]
Viscosity ratio of liquid inside and outside the PEL layer μ_{PEL}/μ_E	1–7	[31]

obtained by the spectral method were generated by setting $l_{\max} = m_{\max} = r_{\max} = q_{\max} = 100$. The presentation of the results starts with studying the electric potential distribution.

The heightwise variation of ψ^* at the vertical centerline for different values of t^* and η_ε is displayed in Fig. 3. The first point to note in this figure is the close agreement between the results of the spectral method and the predictions of the full numerical solution of Eq. (11), in spite of the maximum values of ψ^* being no longer small compared to 1. Therefore, in this regime the Debye-Hückel approximation is still accurate. A thicker PEL is found to provide higher electric potentials. This is expected since the number of fixed-charge groups increases with t^*. Moreover, it is observed that the electric potential increases (especially within the PEL) with increasing the ion partitioning effect, that is, by decreasing η_ε. The underlying physical reason is that the number of anions accumulated to neutralize the fixed-charge groups decreases within the PEL due to the partitioning effect, where the permittivity is lower.

We now turn our attention to the ionic distribution over the channel cross-sectional area. Figure 4 depicts the profiles of the cationic and anionic distributions in a dimensionless form, given as $c^*_\pm = c_\pm/c^\infty$. The partitioning of ions between the two domains, manifesting itself in a discontinuity of the ionic concentration at the PEL/electrolyte interface accompanied by a reduction of the ionic concentration within the PEL, can clearly be observed in this figure. Moreover, it can be seen that the number density of the anions is everywhere larger than the number density of cations, reflecting the fact that positively charged fixed PEL ions have been considered. The anionic/cationic concentration at the channel centerline is a little above/below c^∞, which is a sign of a moderate EDL overlap.

Figure 5 is devoted to the dimensionless velocity profiles for two different values of α. The slope change at the PEL/electrolyte interface is visible in this figure, especially for $\alpha = 1$. The dimensionless Debye-Hückel parameter in this figure is $K = 4$, for which there is a net charge

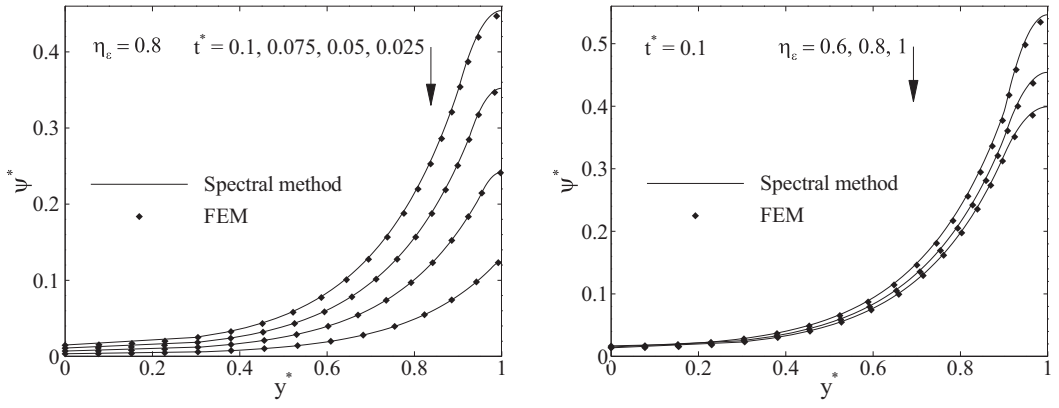

FIG. 3. Heightwise variation of ψ^* at the vertical centerline for different values of t^* and η_ε, while keeping $W^* = 1$ and $K = 5$. The results of the spectral method are compared with the predictions of the full numerical solution of Eq. (11).

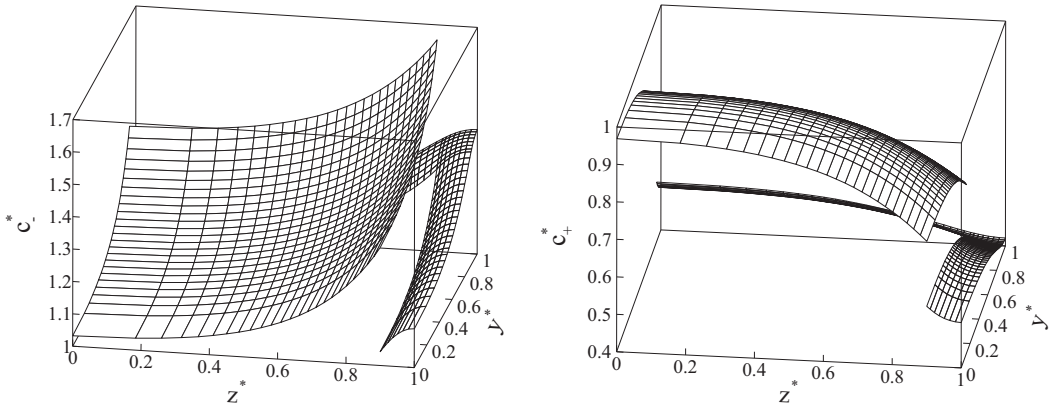

FIG. 4. Cross-sectional distributions of c_-^* and c_+^* for $W^* = 1$, $t^* = 0.1$, $K = 4$, and $\eta_\varepsilon = 0.8$.

everywhere in the liquid, creating a body force over the whole channel area, similar to pressure-driven flow. Accordingly, it is not surprising to see a nearly parabolic velocity profile, typical for Poiseuille flows. The parameter α is a measure of the PEL friction, and a reduction of the fluid velocity, especially within the soft layer, is expected by increasing this parameter, as evidenced by Fig. 5. For $\alpha = 1$, the retarding effect of the PEL is quite small and, hence, the velocity profile is very similar to that established in a duct with rigid walls for which there is no Stokes drag force.

The impacts of the four dimensionless groups t^*, K, η_ε, and η_μ on the velocity distribution along the vertical centerline are investigated via Fig. 6. In part (a) of the figure, the influence of t^* on the velocity profile is studied, indicating that the fluid velocity is enlarged by increasing the PEL thickness. This means that, although a thicker soft layer produces higher friction forces, the increase of the driving force due to the space-charge region overcompensates this effect.

The influence of the EDL thickness on the velocity distribution is studied via Fig. 6(b). To this end, η_λ is varied along with K to keep the PEL charge constant so as to investigate merely the EDL thickness effects. It is observed that the fluid velocity is smaller for a smaller λ_E, corresponding to a larger K. For thick EDLs, like in the case of $K = 4$, the body force exists almost over the entire channel cross section. Since the majority of the body force is applied to the fluid outside the PEL, where there is no Stokes retarding force, comparatively large velocities are achieved. For thinner

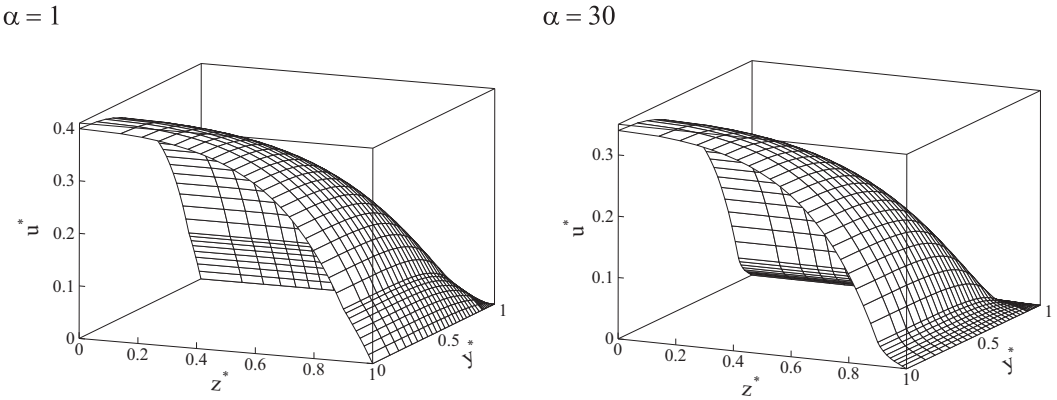

FIG. 5. Profiles of the dimensionless velocity at two different values of α, while keeping $W^* = 1$, $t^* = 0.1$, $K = 4$, $\eta_\varepsilon = 0.8$, and $\eta_\mu = 1.5$.

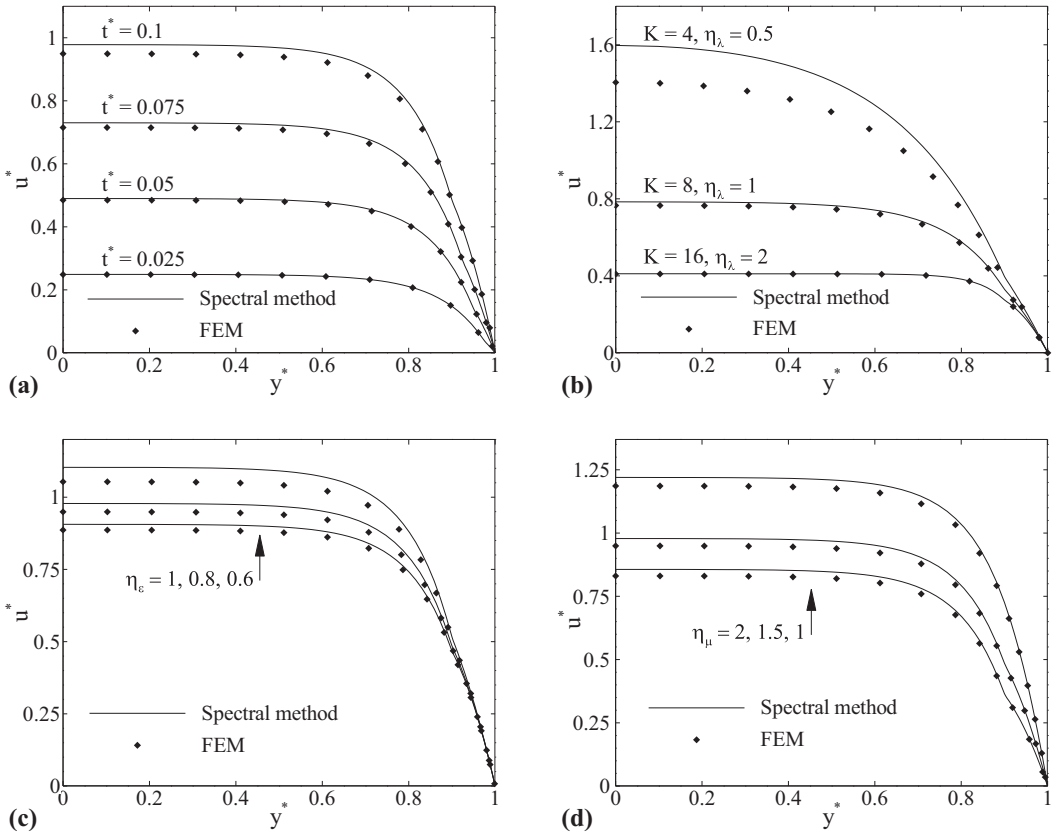

FIG. 6. Heightwise variation of u^* at the vertical centerline for different values of t^*, K (and η_λ), η_ε, and η_μ. The default parameters are $W^* = 1$, $t^* = 0.1$, $K = 10$, $\eta_\varepsilon = 0.8$, $\eta_\mu = 1.5$, and $\alpha = 1$. The results of the spectral method are compared with the predictions of the full numerical solution of Eqs. (11) and (25).

EDLs, however, the body force is mostly limited to the PEL region where the retarding effect of the PEL and the enhanced fluid viscosity prevent a significant fluid flow. Note that the former is more important since a thinner EDL results in lower velocities even when the viscosity ratio is 1. This characteristic of EOF in soft microchannels is quite the opposite of that observed in rigid microchannels where increasing λ_E tends to increase the EDL overlap which in turn reduces the flow velocity [1].

In part (c) of Fig. 6, it is shown that the ion partitioning effect enhances the fluid velocity, a trend that is rather antiintuitive, since the partitioning of ions reduces the ionic concentration within the PEL. However, this reduction is accompanied by an increase of the ionic concentration outside the PEL. This is shown in Fig. 7 that depicts the corresponding net ionic concentrations. The parameter $c_-^* - c_+^*$, displayed in this figure, is a measure of the electroosmotic body force. The net ionic concentration increases in the bulk with decreasing η_ε. This occurs because the number of PEL fixed charges, to be neutralized by the free counterions, is the same for all three cases. Because of the increase of the net ionic concentration outside the PEL where the fluid does not encounter any resistive body force, a noticeable increase in the velocity occurs when lowering η_ε.

Part (d) of Fig. 6 is dedicated to the effects of the viscosity ratio. An increase in η_μ is found to be accompanied by a decrease in the fluid velocity over the entire channel height. This is anticipated, since a larger η_μ corresponds to a larger μ_{PEL} for a given μ_E. Accordingly, the increased viscous force retards the fluid flow. It is worth noting that for $\eta_\mu = 2$, for which there

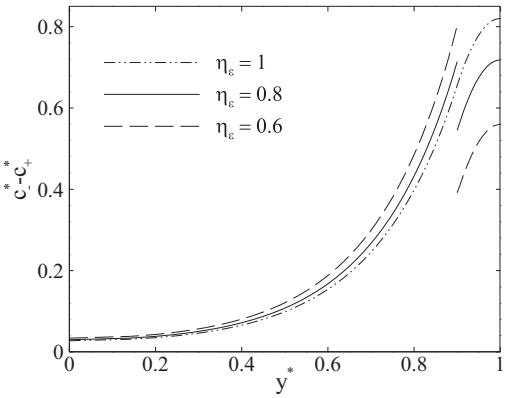

FIG. 7. Heightwise variation of $c^*_- - c^*_+$ at the vertical centerline for different values of η_ε and $W^* = 1$, $t^* = 0.1$, $K = 5$.

is a considerable viscosity contrast between the two domains, the slope change becomes obvious at the PEL/electrolyte interface. The last point worth mentioning regarding Fig. 6 is the relatively good agreement between the results from the spectral method and the full numerical results, especially for low and moderate velocities.

The mean velocity is plotted vs W^* in Fig. 8 for different values of t^*. The special solution for $1 \ll W^*$, which is independent of the aspect ratio, is also shown in this figure. It can be seen that u^*_m increases with W^* and approaches an asymptote. The increase of u^*_m with W^* may be attributed to the fact that the effect of the flow reduction at the corners is smaller for larger W^*. The analytical solution for $1 \ll W^*$ provides acceptable results for $10 \leqslant W^*$. The discrepancy between this solution and the general solution increases when the PEL expands.

The dependence of u^*_m on η_ε, η_μ, and α as obtained from the spectral method and the full numerical solution is displayed in Fig. 9 for different values of the PEL thickness. It is observed that u^*_m is a decreasing function of all these parameters, but the dependence becomes weaker for thinner PELs. This is anticipated since these parameters reflect the PEL properties and, when the PEL shrinks, the flow is mostly affected by the fluid properties outside the soft layer. An interesting

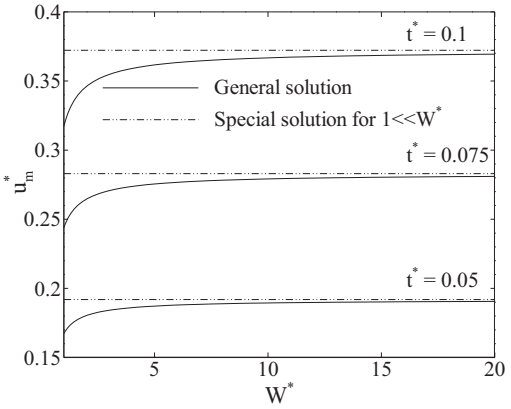

FIG. 8. Dependence of the average velocity on W^* for different values of t^*, while keeping $K = 5$, $\eta_\varepsilon = 0.8$, $\eta_\mu = 1.5$, and $\alpha = 1$. The results of the general solution are compared with the predictions of the special solution for $1 \ll W^*$.

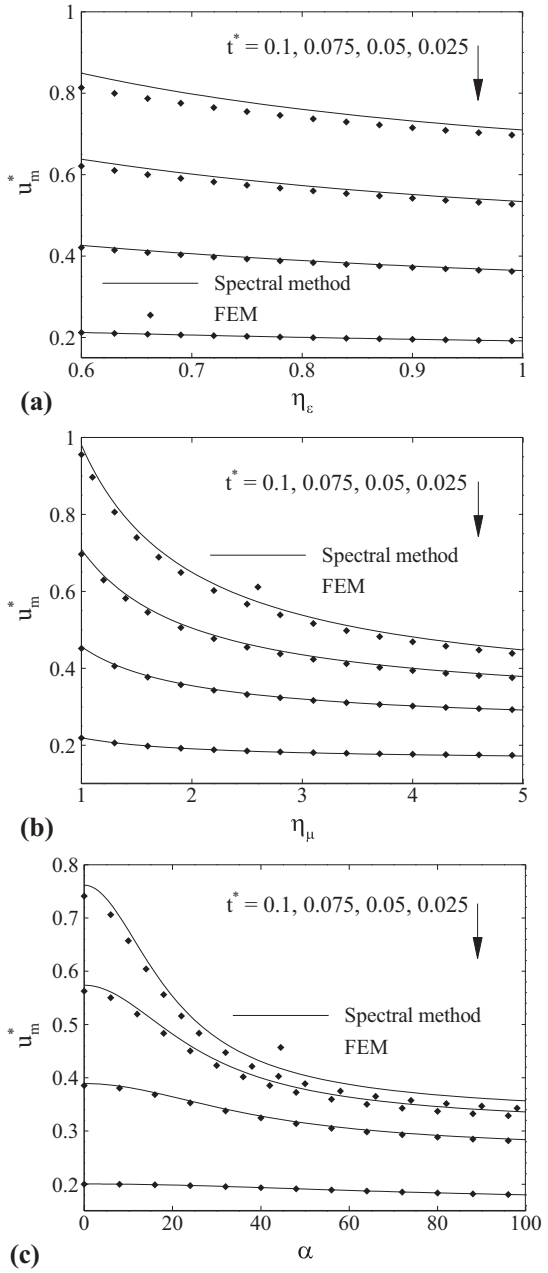

FIG. 9. Dependence of the average velocity on η_ε, η_μ, and α at different values of t^*. The default parameters are $W^* = 1$, $K = 10$, $\eta_\varepsilon = 0.8$, $\eta_\mu = 1.5$, and $\alpha = 1$. The results of the spectral method are compared with the predictions of the full numerical solution of Eqs. (11) and (25).

feature visible in Fig. 9(c) is that the effect of t^* on u_m^* is gradually diminished when α increases. For a physical interpretation of this trend, one should first pay attention to the impact of α on the velocity distribution. As noted previously, for increasing α the intensified resistive force of the PEL retards the fluid flow. In the first place, the retardation effect is limited to the soft layer, and the fluid outside the PEL is only affected indirectly via the viscous force. As such, there is an upper limit for

the influence of α on the mean velocity, which is obtained when the fluid virtually stops flowing in the PEL at high values of α. At this point, any further increase in α leaves the fluid flow outside the soft layer effectively unchanged, resulting in asymptotic values for the mean velocity. It is worth noting that, under these circumstances, there is no shear force between the fluid and the rigid wall, and the electric body force is solely balanced by the PEL retarding force. Concerning the influence of t^* on u_m^*, it can be deduced from the above discussion that thickening the PEL will have two opposite effects on the fluid flow when α is high. First, the region over which there is no fluid flow extends by increasing t^*. Second, the enhanced electric charge of the fixed ions increases the net ionic charge, which leads to the magnification of the flow velocity outside the PEL. Accordingly, there are two effects that partially cancel each other, resulting in a rather weak influence of t^* at large values of α.

Finally, we would like to evaluate some aspects related to the practical relevance of the model presented in this paper. The step change in the physical properties at the PEL/electrolyte implies a discontinuous change of relevant physical quantities such as the mass and charge density or permittivity. Naturally, this represents an idealization. Realistic density/volume fraction profiles of PEL layers have been determined using neutron scattering. PEL brushes grafted to surfaces are often characterized by rather smoothly decaying density profiles that may be approximated by Gaussian distributions [39,40]. However, at high salt concentrations, when electrostatic interactions between the PEL chains are screened, profiles that come close to a step function have been found [41]. Also, PEL multilayers appear to be well described by a step-function profile [42]. The sharp transitions of the quantities shown in Figs. 4 –7, respectively of their gradients, are in fact artifacts of our steplike model of the PEL. How realistic a steplike model will be when local quantities are considered depends on the specific situation, as described above. However, since realistic PEL density/volume fraction profiles can be interpreted as mollified versions of a steplike profile, we expect that global quantities are described quite realistically.

In addition, the model developed neglects some nonlinear effects arising at high flow rates. For example, the polyelectrolyte brushes may deform by the fluid flow when the flow rate is sufficiently high, thereby invalidating the assumption of a prescribed uniform PEL structure. This is particularly true for irreversibly adsorbed PELs which tend to be very deformable.

IV. CONCLUSIONS

The electrostatic potential, ionic concentration, and electroosmotic flow in a soft rectangular microchannel were studied under the condition that considerable differences occur between the values of the physical properties such as permittivity and fluid viscosity inside and outside the PEL. The ion partitioning effect, caused by the permittivity difference between the bulk and the PEL, was taken into account. The flow was assumed to be steady and fully developed, and the PEL properties were considered as constant. Since the classical method of obtaining solutions for the two channel domains followed by matching the solutions is not possible for a rectangular geometry, the problem was handled utilizing a variational approach that treats the whole area under consideration as a single domain with variable physical properties. The solution was obtained based on a spectral method with the aid of the Debye-Hückel linearization and was successfully compared with the predictions of full numerical solutions of the governing nonlinear equations. A closed-form analytical solution was obtained for large ratios of channel width to channel height, where the geometry effectively reduces to a slab bounded by parallel walls. Furthermore, it was demonstrated how charges at the channel walls may be taken into account.

The results indicate that the reduction of the counterions in the PEL caused by the partitioning effect increases the electrostatic potential drop inside the channel, especially within the soft layer. The potential drop is also increased by thickening the PEL. Contrary to expectations, the partitioning of ions amplifies the fluid velocity, because of an amplification of the net ionic concentration outside the PEL. Furthermore, by increasing the channel width for a given height, the mean fluid velocity increases and approaches an asymptotic value. For high aspect ratios the numerically computed

mean velocity is in good agreement with the analytical solution. As expected, lower flow rates are obtained when increasing the fluid viscosity in the PEL for a given bulk viscosity, a trend that is more pronounced for thick PELs. In addition, although increasing the PEL friction reduces the flow rate, at high friction factors the fluid within the PEL virtually stops flowing, with the result that the friction factor no longer affects the flow field. Finally, even though shrinking the EDL results in larger electroosmotic velocities for rigid microchannels [1], the opposite is observed for a PEL-covered microchannel.

At least two major new results were reported in this research work that call for experimental validation: the increase of the volumetric flow rate caused by ion partitioning and the increasing trend of the flow rate with the EDL thickness. The former may be examined by measuring the flow rate in microchannels covered with dense PELs composed of different monomers that cause different degrees of ion partitioning, while the latter may be explored by utilizing different salt concentrations.

ACKNOWLEDGMENT

A. Sadeghi and M. Azari sincerely thank the Iran National Science Foundation (INSF) for their financial support during the course of this work.

The authors declare that they have no conflict of interest.

APPENDIX A: PARAMETERS RELATED TO THE ELECTRIC POTENTIAL DISTRIBUTION

It can be shown that

$$
\begin{aligned}
c_i &= K^2\eta_\lambda^{-2}\left(\int_{\mathbb{A}^*} f_i d\mathbb{A}^* - \int_{\mathbb{A}_E^*} f_i d\mathbb{A}^*\right)\\
&= K^2\eta_\lambda^{-2}W^*\left[\!\!\left[\delta_{0,l_i+m_i} - \left\{\delta_{0,l_i}(1-t^*) + \left(1-\delta_{0,l_i}\right)\frac{\sin\left[\xi_{l_i}(1-t^*)\right]}{\xi_{l_i}+\delta_{0,l_i}}\right\}\right.\right.\\
&\quad\left.\left.\times\left\{\delta_{0,m_i}(1-t^*/W^*) + \left(1-\delta_{0,m_i}\right)\frac{\sin\left[\xi_{m_i}(1-t^*/W^*)\right]}{\xi_{m_i}+\delta_{0,m_i}}\right\}\right]\!\!\right],
\end{aligned}
\tag{A1}
$$

where $t^* = t/H$ denotes the dimensionless PEL thickness and δ is the Kronecker delta. For evaluation of a_{ij}, we first write

$$
\begin{aligned}
a_{ij} &= \eta_\varepsilon\int_{\mathbb{A}^*}\left(\frac{\partial f_i}{\partial y^*}\frac{\partial f_j}{\partial y^*} + \frac{\partial f_i}{\partial z^*}\frac{\partial f_j}{\partial z^*}\right)d\mathbb{A}^* + (1-\eta_\varepsilon)\int_{\mathbb{A}_E^*}\left(\frac{\partial f_i}{\partial y^*}\frac{\partial f_j}{\partial y^*} + \frac{\partial f_i}{\partial z^*}\frac{\partial f_j}{\partial z^*}\right)d\mathbb{A}^*\\
&\quad + K^2\exp\left[\Xi\left(1-\eta_\varepsilon^{-1}\right)\right]\int_{\mathbb{A}^*} f_i f_j d\mathbb{A}^* + K^2\left\{1-\exp\left[\Xi\left(1-\eta_\varepsilon^{-1}\right)\right]\right\}\int_{\mathbb{A}_E^*} f_i f_j d\mathbb{A}^*,
\end{aligned}
\tag{A2}
$$

where $\eta_\varepsilon = \varepsilon_{\mathrm{PEL}}/\varepsilon_E$. Performing the integrations in Eq. (A2), the final expression of a_{ij} is obtained as

$$
\begin{aligned}
a_{ij} &= \frac{\eta_\varepsilon}{4W^*}\delta_{l_i,l_j}\delta_{m_i,m_j}\left[W^{*2}\xi_{l_i}\xi_{l_j}\left(1+\delta_{0,m_i+m_j}\right) + \xi_{m_i}\xi_{m_j}\left(1+\delta_{0,l_i+l_j}\right)\right]\\
&\quad + \frac{1-\eta_\varepsilon}{4W^*}\left[\!\!\left[W^{*2}\xi_{l_i}\xi_{l_j}\left[\!\!\left[\delta_{l_i,l_j}\left\{1-t^* - \frac{\sin\left[2\xi_{l_i}(1-t^*)\right]}{2\xi_{l_i}+\delta_{0,l_i}}\right\}\right.\right.\right.\right.\\
&\quad\left.\left.\left.\left. + \left(1-\delta_{l_i,l_j}\right)\left\{\frac{\sin\left[\left(\xi_{l_i}-\xi_{l_j}\right)(1-t^*)\right]}{\xi_{l_i}-\xi_{l_j}+\delta_{l_i,l_j}} - \frac{\sin\left[\left(\xi_{l_i}+\xi_{l_j}\right)(1-t^*)\right]}{\xi_{l_i}+\xi_{l_j}+\delta_{0,l_i+l_j}}\right\}\right]\!\!\right]\right.\right.
\end{aligned}
$$

$$
\begin{aligned}
&\times \Bigg[\Bigg[2\delta_{0,m_i+m_j}(1-t^*/W^*)+\delta_{m_i,m_j}\big(1-\delta_{0,m_i+m_j}\big)\Bigg\{1-t^*/W^*+\frac{\sin\big[2\xi_{m_i}(1-t^*/W^*)\big]}{2\xi_{m_i}+\delta_{0,m_i}}\Bigg\}\\
&+\big(1-\delta_{m_i,m_j}\big)\Bigg\{\frac{\sin\big[(\xi_{m_i}-\xi_{m_j})(1-t^*/W^*)\big]}{\xi_{m_i}-\xi_{m_j}+\delta_{m_i,m_j}}+\frac{\sin\big[(\xi_{m_i}+\xi_{m_j})(1-t^*/W^*)\big]}{\xi_{m_i}+\xi_{m_j}+\delta_{0,m_i+m_j}}\Bigg\}\Bigg]\\
&+\xi_{m_i}\xi_{m_j}\Bigg[2\delta_{0,l_i+l_j}(1-t^*)+\delta_{l_i,l_j}\big(1-\delta_{0,l_i+l_j}\big)\Bigg\{1-t^*+\frac{\sin\big[2\xi_{l_i}(1-t^*)\big]}{2\xi_{l_i}+\delta_{0,l_i}}\Bigg\}\\
&+\big(1-\delta_{l_i,l_j}\big)\Bigg\{\frac{\sin\big[(\xi_{l_i}-\xi_{l_j})(1-t^*)\big]}{\xi_{l_i}-\xi_{l_j}+\delta_{l_i,l_j}}+\frac{\sin\big[(\xi_{l_i}+\xi_{l_j})(1-t^*)\big]}{\xi_{l_i}+\xi_{l_j}+\delta_{0,l_i+l_j}}\Bigg\}\Bigg]\\
&\times \Bigg[\Bigg[\delta_{m_i,m_j}\Bigg\{1-t^*/W^*-\frac{\sin\big[2\xi_{m_i}(1-t^*/W^*)\big]}{2\xi_{m_i}+\delta_{0,m_i}}\Bigg\}\\
&+\big(1-\delta_{m_i,m_j}\big)\Bigg\{\frac{\sin\big[(\xi_{m_i}-\xi_{m_j})(1-t^*/W^*)\big]}{\xi_{m_i}-\xi_{m_j}+\delta_{m_i,m_j}}-\frac{\sin\big[(\xi_{m_i}+\xi_{m_j})(1-t^*/W^*)\big]}{\xi_{m_i}+\xi_{m_j}+\delta_{0,m_i+m_j}}\Bigg\}\Bigg]\Bigg]\\
&+\frac{K^2W^*}{4}\exp\big[\Xi\big(1-\eta_\varepsilon^{-1}\big)\big]\delta_{l_i,l_j}\delta_{m_i,m_j}\big(1+\delta_{0,m_i+m_j}\big)\big(1+\delta_{0,l_i+l_j}\big)\\
&+\frac{K^2W^*}{4}\big\{1-\exp\big[\Xi\big(1-\eta_\varepsilon^{-1}\big)\big]\big\}\\
&\times \Bigg[\Bigg[2\delta_{0,l_i+l_j}(1-t^*)+\delta_{l_i,l_j}\big(1-\delta_{0,l_i+l_j}\big)\Bigg\{1-t^*+\frac{\sin\big[2\xi_{l_i}\big(1-t^*\big)\big]}{2\xi_{l_i}+\delta_{0,l_i}}\Bigg\}\\
&+\big(1-\delta_{l_i,l_j}\big)\Bigg\{\frac{\sin\big[(\xi_{l_i}-\xi_{l_j})(1-t^*)\big]}{\xi_{l_i}-\xi_{l_j}+\delta_{l_i,l_j}}+\frac{\sin\big[(\xi_{l_i}+\xi_{l_j})(1-t^*)\big]}{\xi_{l_i}+\xi_{l_j}+\delta_{0,l_i+l_j}}\Bigg\}\Bigg]\\
&\times \Bigg[\Bigg[2\delta_{0,m_i+m_j}(1-t^*/W^*)+\delta_{m_i,m_j}\big(1-\delta_{0,m_i+m_j}\big)\Bigg\{1-t^*/W^*+\frac{\sin\big[2\xi_{m_i}(1-t^*/W^*)\big]}{2\xi_{m_i}+\delta_{0,m_i}}\Bigg\}\\
&+\big(1-\delta_{m_i,m_j}\big)\Bigg\{\frac{\sin\big[(\xi_{m_i}-\xi_{m_j})(1-t^*/W^*)\big]}{\xi_{m_i}-\xi_{m_j}+\delta_{m_i,m_j}}+\frac{\sin\big[(\xi_{m_i}+\xi_{m_j})(1-t^*/W^*)\big]}{\xi_{m_i}+\xi_{m_j}+\delta_{0,m_i+m_j}}\Bigg\}\Bigg]\Bigg]. \qquad \text{(A3)}
\end{aligned}
$$

APPENDIX B: PARAMETERS RELATED TO THE VELOCITY DISTRIBUTION

Performing the integration in Eq. (36), it is shown that

$$
\begin{aligned}
h_i &= K^2\exp\big[\Xi\big(1-\eta_\varepsilon^{-1}\big)\big]\int_{\mathbb{A}^*}\psi^* g_i d\mathbb{A}^* + K^2\big\{1-\exp\big[\Xi\big(1-\eta_\varepsilon^{-1}\big)\big]\big\}\int_{\mathbb{A}_E^*}\psi^* g_i d\mathbb{A}^*\\
&= K^2\exp\big[\Xi\big(1-\eta_\varepsilon^{-1}\big)\big]\sum_{j=1}^{M}\frac{W^* b_j}{4}\Bigg[\frac{(-1)^{r_i-l_j}}{\xi_{r_i}-\xi_{l_j}}+\frac{(-1)^{r_i+l_j}}{\xi_{r_i}+\xi_{l_j}}\Bigg]\Bigg[\frac{(-1)^{q_i-m_j}}{\xi_{q_i}-\xi_{m_j}}+\frac{(-1)^{q_i+m_j}}{\xi_{q_i}+\xi_{m_j}}\Bigg]\\
&\quad+K^2\big\{1-\exp\big[\Xi\big(1-\eta_\varepsilon^{-1}\big)\big]\big\}\sum_{j=1}^{M}\frac{W^* b_j}{4}\Bigg\{\frac{\sin\big[(\xi_{r_i}-\xi_{l_j})(1-t^*)\big]}{\xi_{r_i}-\xi_{l_j}}+\frac{\sin\big[(\xi_{r_i}+\xi_{l_j})(1-t^*)\big]}{\xi_{r_i}+\xi_{l_j}}\Bigg\}\\
&\quad\times\Bigg\{\frac{\sin\big[(\xi_{q_i}-\xi_{m_j})(1-t^*/W^*)\big]}{\xi_{q_i}-\xi_{m_j}}+\frac{\sin\big[(\xi_{q_i}+\xi_{m_j})(1-t^*/W^*)\big]}{\xi_{q_i}+\xi_{m_j}}\Bigg\}. \qquad \text{(B1)}
\end{aligned}
$$

For calculation of e_{ij}, we first write

$$e_{ij} = \eta_\mu \int_{\mathbb{A}^*} \left(\frac{\partial g_i}{\partial y^*}\frac{\partial g_j}{\partial y^*} + \frac{\partial g_i}{\partial z^*}\frac{\partial g_j}{\partial z^*} \right) d\mathbb{A}^* + (1-\eta_\mu) \int_{\mathbb{A}_E^*} \left(\frac{\partial g_i}{\partial y^*}\frac{\partial g_j}{\partial y^*} + \frac{\partial g_i}{\partial z^*}\frac{\partial g_j}{\partial z^*} \right) d\mathbb{A}^* + \alpha^2 \left(\int_{\mathbb{A}^*} g_i g_j d\mathbb{A}^* - \int_{\mathbb{A}_E^*} g_i g_j d\mathbb{A}^* \right), \tag{B2}$$

where $\eta_\mu = \mu_{\mathrm{PEL}}/\mu_E$. Carrying out the integrations in Eq. (B2), e_{ij} is determined as

$$\begin{aligned}
e_{ij} = {} & \frac{\eta_\mu \delta_{r_i,r_j}\delta_{q_i,q_j}}{4W^*}\left(W^{*2}\xi_{r_i}\xi_{r_j} + \xi_{q_i}\xi_{q_j}\right) + (1-\eta_\mu)\frac{W^*\xi_{r_i}\xi_{r_j}}{4}\left[\!\!\left[\delta_{r_i,r_j}\left\{1 - t^* - \frac{\sin\left[2\xi_{r_i}(1-t^*)\right]}{2\xi_{r_i}}\right\}\right.\right. \\
& \left.\left. + \left(1-\delta_{r_i,r_j}\right)\left\{\frac{\sin\left[\left(\xi_{r_i}-\xi_{r_j}\right)(1-t^*)\right]}{\xi_{r_i}-\xi_{r_j}+\delta_{r_i,r_j}} - \frac{\sin\left[\left(\xi_{r_i}+\xi_{r_j}\right)(1-t^*)\right]}{\xi_{r_i}+\xi_{r_j}}\right\}\right]\!\!\right] \\
& \times \left[\!\!\left[\delta_{q_i,q_j}\left\{1 - t^*/W^* + \frac{\sin\left[2\xi_{q_i}(1-t^*/W^*)\right]}{2\xi_{q_i}}\right\}\right.\right. \\
& \left.\left. + \left(1-\delta_{q_i,q_j}\right)\left\{\frac{\sin\left[\left(\xi_{q_i}-\xi_{q_j}\right)(1-t^*/W^*)\right]}{\xi_{q_i}-\xi_{q_j}+\delta_{q_i,q_j}} + \frac{\sin\left[\left(\xi_{q_i}+\xi_{q_j}\right)(1-t^*/W^*)\right]}{\xi_{q_i}+\xi_{q_j}}\right\}\right]\!\!\right] \\
& + (1-\eta_\mu)\frac{\xi_{q_i}\xi_{q_j}}{4W^*}\left[\!\!\left[\delta_{r_i,r_j}\left\{1 - t^* + \frac{\sin\left[2\xi_{r_i}(1-t^*)\right]}{2\xi_{r_i}}\right\}\right.\right. \\
& \left.\left. + \left(1-\delta_{r_i,r_j}\right)\left\{\frac{\sin\left[\left(\xi_{r_i}-\xi_{r_j}\right)(1-t^*)\right]}{\xi_{r_i}-\xi_{r_j}+\delta_{r_i,r_j}} + \frac{\sin\left[\left(\xi_{r_i}+\xi_{r_j}\right)(1-t^*)\right]}{\xi_{r_i}+\xi_{r_j}}\right\}\right]\!\!\right] \\
& \times \left[\!\!\left[\delta_{q_i,q_j}\left\{1 - t^*/W^* - \frac{\sin\left[2\xi_{q_i}(1-t^*/W^*)\right]}{2\xi_{q_i}}\right\}\right.\right. \\
& \left.\left. + \left(1-\delta_{q_i,q_j}\right)\left\{\frac{\sin\left[\left(\xi_{q_i}-\xi_{q_j}\right)(1-t^*/W^*)\right]}{\xi_{q_i}-\xi_{q_j}+\delta_{q_i,q_j}} - \frac{\sin\left[\left(\xi_{q_i}+\xi_{q_j}\right)(1-t^*/W^*)\right]}{\xi_{q_i}+\xi_{q_j}}\right\}\right]\!\!\right] \\
& + \frac{\alpha^2}{4}W^*\delta_{r_i,r_j}\delta_{q_i,q_j} - \frac{\alpha^2}{4}W^*\left[\!\!\left[\delta_{r_i,r_j}\left\{1 - t^* + \frac{\sin\left[2\xi_{r_i}(1-t^*)\right]}{2\xi_{r_i}}\right\}\right.\right. \\
& \left.\left. + \left(1-\delta_{r_i,r_j}\right)\left\{\frac{\sin\left[\left(\xi_{r_i}-\xi_{r_j}\right)(1-t^*)\right]}{\xi_{r_i}-\xi_{r_j}+\delta_{r_i,r_j}} + \frac{\sin\left[\left(\xi_{r_i}+\xi_{r_j}\right)(1-t^*)\right]}{\xi_{r_i}+\xi_{r_j}}\right\}\right]\!\!\right] \\
& \times \left[\!\!\left[\delta_{q_i,q_j}\left\{1 - t^*/W^* + \frac{\sin\left[2\xi_{q_i}(1-t^*/W^*)\right]}{2\xi_{q_i}}\right\}\right.\right. \\
& \left.\left. + \left(1-\delta_{q_i,q_j}\right)\left\{\frac{\sin\left[\left(\xi_{q_i}-\xi_{q_j}\right)(1-t^*/W^*)\right]}{\xi_{q_i}-\xi_{q_j}+\delta_{q_i,q_j}} + \frac{\sin\left[\left(\xi_{q_i}+\xi_{q_j}\right)(1-t^*/W^*)\right]}{\xi_{q_i}+\xi_{q_j}}\right\}\right]\!\!\right].
\end{aligned} \tag{B3}$$

[1] J. H. Masliyah and S. Bhattacharjee, *Electrokinetic and Colloid Transport Phenomena*, 1st ed. (Wiley, New Jersey, 2006).
[2] X. Wang, S. Wang, B. Gendhar, C. Cheng, C. K. Byun, G. Li, M. Zhao, and S. Liu, Electroosmotic pumps for microflow analysis, Trends Anal. Chem. **28**, 64 (2009).
[3] V. Hoshyargar, A. Khorami, S. N. Ashrafizadeh, and A. Sadeghi, Solute dispersion by electroosmotic flow through soft microchannels, Sens. Actuators, B **255**, 3585 (2018).
[4] D. Li, *Electrokinetics in Microfluidics* (Elsevier, Amsterdam, 2004).
[5] H. Ohshima, Theory of electrostatics and electrokinetics of soft particles, Sci. Technol. Adv. Mater. **10**, 063001 (2009).
[6] S. T. Milner, Polymer brushes, Science **251**, 905 (1991).
[7] H. S. Gaikwad, P. K. Mondal, and S. Wongwises, Softness induced enhancement in net throughput of non-linear bio-fluids in nanofluidic channel under EDL phenomenon, Sci. Rep. **8**, 7893 (2018).
[8] J. F. L. Duval, D. Küttner, C. Werner, and R. Zimmermann, Electrohydrodynamics of soft polyelectrolyte multilayers: Point of zero-streaming current, Langmuir **27**, 10739 (2011).
[9] E. Donath and A. Voigt, Streaming current and streaming potential on structured surfaces, J. Colloid Interface Sci. **109**, 122 (1986).
[10] H. Ohshima and T. Kondo, Electrokinetic flow between two parallel plates with surface charge layers: Electro-osmosis and streaming potential, J. Colloid Interface Sci. **135**, 443 (1990).
[11] V. M. Starov and Y. E. Solomentsev, Influence of gel layers on electrokinetic phenomena: 1. Streaming potential, J. Colloid Interface Sci. **158**, 159 (1993).
[12] H. J. Keh and Y. C. Liu, Electrokinetic flow in a circular capillary with a surface charge layer, J. Colloid Interface Sci. **172**, 222 (1995).
[13] J. L. Harden, D. Long, and A. Ajdari, Influence of end-grafted polyelectrolytes on electro-osmosis along charged surfaces, Langmuir **17**, 705 (2001).
[14] H. J. Keh and J. M. Ding, Electrokinetic flow in a capillary with a charge-regulating surface polymer layer, J. Colloid Interface Sci. **263**, 645 (2003).
[15] S. S. Dukhin, R. Zimmermann, and C. Werner, Intrinsic charge and Donnan potentials of grafted polyelectrolyte layers determined by surface conductivity data, J. Colloid Interface Sci. **274**, 309 (2004).
[16] S. S. Dukhin, R. Zimmermann, and C. Werner, Electrokinetic phenomena at grafted polyelectrolyte layers, J. Colloid Interface Sci. **286**, 761 (2005).
[17] R. Qiao, Control of electroosmotic flow by polymer coating: Effects of the electrical double layer, Langmuir **22**, 7096 (2006).
[18] J. F. L. Duval, R. Zimmermann, A. L. Cordeiro, N. Rein, and C. Werner, Electrokinetics of diffuse soft interfaces. IV. Analysis of streaming current measurements at thermoresponsive thin films, Langmuir **25**, 10691 (2009).
[19] R. Zimmermann, S. S. Dukhin, C. Werner, and J. F. L. Duval, On the use of electrokinetics for unraveling charging and structure of soft planar polymer films, Curr. Opin. Colloid Interface Sci. **18**, 83 (2013).
[20] L.-H. Yeh, M. Zhang, N. Hu, S. W. Joo, S. Qian, and J.-P. Hsu, Electrokinetic ion and fluid transport in nanopores functionalized by polyelectrolyte brushes, Nanoscale **4**, 5169 (2012).
[21] L. Benson, L.-H. Yeh, T.-H. Chou, and S. Qian, Field effect regulation of Donnan potential and electrokinetic flow in a functionalized soft nanochannel, Soft Matter **9**, 9767 (2013).
[22] C. Zhou, L. Mei, Y.-S. Su, L.-H. Yeh, X. Zhang, and S. Qian, Gated ion transport in a soft nanochannel with biomimetic polyelectrolyte brush layers, Sens. Actuators, B **229**, 305 (2016).
[23] F. Li, Y. Jian, Z. Xie, Y. Liu, and Q. Liu, Transient alternating current electroosmotic flow of a Jeffrey fluid through a polyelectrolyte-grafted nanochannel, RSC Adv. **7**, 782 (2017).
[24] U. Marini Bettolo Marconi, M. Monteferrante, and S. Melchionna, Electro-osmotic flow in coated nanocapillaries: A theoretical investigation, Phys. Chem. Chem. Phys. **16**, 25473 (2014).
[25] M. Monteferrante, S. Melchionna, U. M. B. Marconi, M. Cretich, M. Chiari, and L. Sola, Electroosmotic flow in polymer-coated slits: A joint experimental/simulation study, Microfluid. Nanofluid. **18**, 475 (2015).
[26] J.-Y. Lin, C.-Y. Lin, J.-P. Hsu, and S. Tseng, Ionic current rectification in a pH-tunable polyelectrolyte brushes functionalized conical nanopore: Effect of salt gradient, Anal. Chem. **88**, 1176 (2016).

[27] A. Sadeghi, Theoretical modeling of electroosmotic flow in soft microchannels: A variational approach applied to the rectangular geometry, Phys. Fluids **30**, 032004 (2018).
[28] A. Poddar, D. Maity, A. Bandopadhyay, and S. Chakraborty, Electrokinetics in polyelectrolyte grafted nanofluidic channels modulated by the ion partitioning effect, Soft Matter **12**, 5968 (2016).
[29] A. Ganjizade, A. Sadeghi, and S. N. Ashrafizadeh, Effect of ion partitioning on electrostatics of soft particles with volumetrically charged inner core coated with pH-regulated polyelectrolyte layer, Colloids Surf., B **170**, 129 (2018).
[30] N. Idota, A. Kikuchi, J. Kobayashi, K. Sakai, and T. Okano, Microfluidic valves comprising nanolayered thermoresponsive polymer-grafted capillaries, Adv. Mater. **17**, 2723 (2005).
[31] D. I. Dimitrov, A. Milchev, and K. Binder, Local viscosity in the vicinity of a wall coated by polymer brush from Green–Kubo relations, Macromol. Theory Simul. **17**, 313 (2008).
[32] H. A. Stone, A. D. Stroock, and A. Ajdari, Engineering flows in small devices: Microfluidics toward a lab-on-a-chip, Ann. Rev. Fluid Mech. **36**, 381 (2004).
[33] H. G. L. Coster, The double fixed charge membrane: Solution-membrane ion partition effects and membrane potentials, Biophys. J. **13**, 133 (1973).
[34] A. Ganjizade, S. N. Ashrafizadeh, and A. Sadeghi, Effect of ion partitioning on the electrostatics of soft particles with a volumetrically charged core, Electrochem. Commun. **84**, 19 (2017).
[35] G. S. Manning, Limiting laws and counterion condensation in polyelectrolyte solutions I. Colligative properties, J. Chem. Phys. **51**, 924 (1969).
[36] H. P. Hsu and E. Lee, Counterion condensation of a polyelectrolyte, Electrochem. Commun. **15**, 59 (2012).
[37] K. Rektorys, *Variational Methods in Mathematics, Science and Engineering*, 2nd ed. (D. Reidel Publishing, Dordrecht, 1980).
[38] H. J. Weber and G. B. Arfken, *Essential Mathematical Methods for Physicists* (Academic, San Diego, 2003).
[39] Y. Mir, P. Auroy, and L. Auvray, Density Profile of Polyelectrolyte Brushes, Phys. Rev. Lett. **75**, 2863 (1995).
[40] M. Moglianetti, J. R. P. Webster, S. Edmondson, S. P. Armes, and S. Titmuss, Neutron reflectivity study of the structure of pH-responsive polymer brushes grown from a macroinitiator at the sapphire-water interface, Langmuir **26**, 12684 (2010).
[41] Y. Tran, P. Auroy, and L. T. Lee, Determination of the structure of polyelectrolyte brushes, Macromolecules **32**, 8952 (1999).
[42] I. Estrela-Lopis, S. Leporatti, S. Moya, A. Brandt, E. Donath, and H. Möhwald, SANS studies of polyelectrolyte multilayers on colloidal templates, Langmuir **18**, 7861 (2002).
[43] S. M. Louie, T. Phenrat, M. J. Small, R. D. Tilton, and G. V. Lowry, Parameter identifiability in application of soft particle electrokinetic theory to determine polymer and polyelectrolyte coating thicknesses on colloids, Langmuir **28**, 10334 (2012).
[44] M. Yang and K. Zhao, Influence of the structure on the collapse of poly(*N*-isopropylacrylamide)-based microgels: An insight by quantitative dielectric analysis, Soft Matter **12**, 4093 (2016).
[45] M. Yang, C. Liu, Y. Lian, K. Zhao, D. Zhu, and J. Zhou, Relaxations and phase transitions during the collapse of a dense PNIPAM microgel suspension—Thorough insight using dielectric spectroscopy, Soft Matter **13**, 2663 (2017).